remote sensing

Article

Detecting Flooded Areas Using Sentinel-1 SAR Imagery

Francisco Alonso-Sarria *, Carmen Valdivieso-Ros and Gabriel Molina-Pérez

Water and Environment Institute, University of Murcia, 30100 Murcia, Spain; mcarmen.valdivieso@um.es (C.V.-R.); gabriel.molina@um.es (G.M.-P.)
* Correspondence: alonsarp@um.es

Abstract: Floods are a major threat to human life and economic assets. Monitoring these events is therefore essential to quantify and minimize such losses. Remote sensing has been used to extract flooded areas, with SAR imagery being particularly useful as it is independent of weather conditions. This approach is more difficult when detecting flooded areas in semi-arid environments, without a reference permanent water body, than when monitoring the water level rise of permanent rivers or lakes. In this study, Random Forest is used to estimate flooded cells after 19 events in Campo de Cartagena, an agricultural area in SE Spain. Sentinel-1 SAR metrics are used as predictors and irrigation ponds as training areas. To minimize false positives, the pre- and post-event results are compared and only those pixels with a probability of water increase are considered as flooded areas. The ability of the RF model to detect water surfaces is demonstrated (mean accuracy = 0.941, standard deviation = 0.048) along the 19 events. Validating using optical imagery (Sentinel-2 MSI) reduces accuracy to 0.642. This form of validation can only be applied to a single event using a S2 image taken 3 days before the S1 image. A large number of false negatives is then expected. A procedure developed to correct for this error gives an accuracy of 0.886 for this single event. Another form of indirect validation consists in relating the area flooded in each event to the amount of rainfall recorded. An RF regression model using both rainfall metrics and season of the year gives a correlation coefficient of 0.451 and RMSE = 979 ha using LOO-CV. This result shows a clear relationship between flooded areas and rainfall metrics.

Keywords: SAR; Sentinel-1; Sentinel-2; flooded areas; machine learing; shapley

check for updates

Academic Editor: Marios Anagnostou

Received: 28 February 2025
Revised: 27 March 2025
Accepted: 8 April 2025
Published: 11 April 2025

Citation: Alonso-Sarria, F.; Valdivieso-Ros, C.; Molina-Pérez, G. Detecting Flooded Areas Using Sentinel-1 SAR Imagery. *Remote Sens.* **2025**, *17*, 1368. https://doi.org/10.3390/rs17081368

1. Introduction

Floods are a major threat to human life and economic property [1–4]. In the last decades, the frequency of floods has increased due to climate change [5,6]. Semi-arid Mediterranean regions have historically experienced recurrent alternations between droughts and floods of low or moderate intensity to which they have adapted over time. However, climate change has led to an increase in the frequency and severity of these events, and climate projections show an upward trend [7]. The Emergency Events Database (EM-DAT) recorded more than 30 million people affected by torrential floods in 2023, with an estimated average annual economic loss of more than USD 41 billion [8]. In semi-arid areas, their severity can be locally amplified by factors related to geography, geology, or hydrology, as well as others such as land management [9]. According to the literature review conducted in [9], these particular characteristics not only distinguish semi-arid floodplains from those of humid regions, but also complicate flood risk management. In addition, there are still technical issues to be resolved, such as the availability of appropriate data during or shortly after events, which leads to modelling problems, among others.

Flood monitoring is essential to quantify and minimize losses of various kinds [10]. The use of remote sensing to extract flooded areas is an essential step in effective flood disaster monitoring, as it can provide the spatio-temporal distribution of flood water with different spatial resolutions in near real time [11]. In this way, frequently flooded areas can be efficiently monitored [12,13]. Several approaches have been proposed to perform this task.

Water indices based on the difference between water and non-water in multispectral optical images include the Normalized Difference Water Index (NDWI) [14], the Modified NDWI (MNDWI) [15–18], the Enhanced Water Index (EWI) [19], or the Automated Water Extraction Index [20]. Other approaches based on optical images are single-band thresholding [21] and thematic classification methods [22,23]. Even combinations of different methods have been proposed [24–27]. The obvious drawback of these approaches is the limitation imposed by clouds on the use of optical bands [28], a particularly important issue when trying to detect flooded surfaces.

SAR imagery, on the other hand, is an important data source for monitoring water surface dynamics due to its ability to penetrate clouds in all weather conditions [29–34]. In particular, Sentinel-1A SAR (S1A) imagery has a high spatio-temporal resolution [35] and therefore a great potential for its use in surface water research. SAR images also have better contrast than optical images and richer texture information [36]; they can be used to detect ground surface properties such as surface roughness and dielectric constant [37]. These geophysical responses and the lateral geometric structure of the SAR system lead to different backscattering mechanisms in different land cover types, making it possible to classify different flooding situations [38,39]. Due to its ability to penetrate vegetation, SAR is better able to identify water and wetlands under vegetation canopies than optical remote sensing [40,41].

Mahdavi et al. (2018) and Gstaiger et al. (2012) concluded that HH polarization and the ascending mode have the greatest potential for water detection [21,42]; however, the primary acquisition mode of the Sentinel-1 mission only supports VV and VH dual-polarization operations [35]. Under VH polarization, the classification of water and non-water in the backscatter coefficient maps is easily confused, and the segmentation of ground objects is stronger than under VV polarization [11]. Although the SAR images with VV polarization are more sensitive to moisture information, VV polarization images are able to show the moisture information of land cover types such as swamps and rice fields more clearly [43], which makes the difference between water and non-water pixels on the images smaller and the contrast less obvious. The contribution rate of the backscatter coefficient features under VH polarization is stronger than under VV polarization. Therefore, in areas with more vegetation and complex ground object types, VH polarization should be more helpful in extracting flooded areas [11]. In this last work, the authors used several new features calculated from VV and VH: VV+VH, VV-VH and VV/VH. Tian et al. (2017) used VV^2, VH^2, and VVVH together with VV and VH in a stepwise regression method to obtain a Sentinel1-A Water Index (SWI) [44].

Initially, SAR-based flood extent mapping methods were simple visual interpretation [45]. Other approaches include interferometric SAR coherence [46], histogram thresholding [47–53], or supervised classification [54–56]. Threshold methods are the most common water extraction algorithms based on the backscatter coefficient of water, which is quite low compared to other objects in SAR data [28]. However, thresholding can be subjective and can vary with time and space [57]. Current automatic thresholding methods include the method in [58] and the entropy thresholding method [59,60]. Threshold methods assume a bimodal histogram of the SAR image; however, if the proportion of water in the image is minimal, the bimodality may not be evident in the histogram, leading to unsatisfactory water extraction results [28]. In addition, the edge of water bodies may be blurred because this method fails to distinguish mixed pixels [28]. However, it is difficult to obtain appropriate thresholds in different periods and regions [44]. Several machine learning models have been used in supervised classification: Random Forest [11,61], support vector machines (SVMs) [62], and artificial neural networks [63]. Some researchers have proposed a manual post-processing step supported by auxiliary data to improve the resulting accuracy [11,63,64]. However, these procdures limit the applicability and automation of the proposed methods [34].

Several algorithms are available for mapping flash floods during a crisis [21,65–70]. For example, Pulvirenti et al. (2011) presented a method combining segmentation techniques and a SAR backscatter model [70]. Matgen et al. (2011) presented a SAR-based flood mapping technique that combines thresholding and region growing [71]. In order to monitor floods more accurately, more advanced studies should focus on the efficient use of multi-temporal (before and during/after the flood) and multi-source data [72]. Other studies focus on monitoring changes in the extent of water bodies, e.g., Cazals et al. (2016) detected the hydrological dynamics of a coastal marsh located in the Regional Natural Park on the French Atlantic coast using the threshold method with S1A data, with an overall accuracy of 82% [73].

Surface water mapping errors are usually due to the high similarity of surface water and non-water features. Two strategies are commonly used to improve surface water mapping, namely (1) enhancing the easily confused/most important water information and (2) suppressing the complex/most important non-water information from an image. In the former case, significant improvement has been achieved in previous research by enhancing the main surface water bodies in a study region, such as lakes [74,75], rivers [76,77], and coastal water areas [78,79]. In the latter case, many studies have achieved significant improvements by suppressing complex/large non-water surfaces, such as built-up areas [15], terrain shadows and other non-water dark surfaces [20,80], and clouds and cloud shadow information [81].

Most of these methods are pixel-based, i.e., only the information in the individual pixel is considered, ignoring features such as texture, shape, relationship between adjacent pixels, and spatial location of ground objects, which are also prone to speckle interference [11]. The object-based image analysis method overcomes this limitation by combining adjacent pixels with homogeneous spectra and textures into a connected region through specific computational rules, and then integrating the averaged spectral and textural features with the spatial relationships of the objects with their neighborhood [11,82]. Therefore, object-based image analysis has become a very effective method for image classification and is increasingly used for flood information extraction [83,84]. However, object-based image analysis works better when the pixel size of the image is smaller than the size of the objects to be identified and when the goal is to monitor changes in the size of water objects.

Recently, deep convolutional neural networks have been introduced. Isikdogan et al. (2017, 2019) proposed a fully convolutional neural network called DeepWaterMap [85,86]. This new structured model can separate surface water from land, snow, ice, clouds, and shadows. Li et al. (2019) introduced a fully convolutional network (FCN) model for water body extraction using very-high-spatial-resolution (VHR) optical imagery [39]. Fang et al. (2019) introduced a ConvNet-based framework to identify reservoirs on a global scale [87]. Compared to traditional methods, deep learning methods have shown superiority and great potential for surface water mapping.

However, deep learning methods require large amounts of labelled data and computational resources, which has prevented their widespread application [88]. The transfer use of state-of-the-art deep models [39,87] and the structural fine-tuning of classical models [85,89] still lack sufficient adaptation to satellite image-based surface water mapping tasks, resulting in models with limited accuracy [88]. In addition, the convolutional approach of CNN has the disadvantage of working well in the core of the objects but having problems at the boundaries. If validation regions are only extracted from the core of the objects, the accuracy will be overestimated.

Validation is difficult when analyzing areas inundated by flash floods. It is possible to use an RGB composition from a post-event image to manually digitize flooded and non-flooded areas. However, it is rare to find a cloud-free optical image close in time to the classified SAR image. Even a delay of one day can result in a large reduction in water coverage due to infiltration or evaporation.

The objective of this study is to develop a methodology to detect water surfaces after 19 flood events in a semi-arid agricultural area, combining a Random Forest model trained on SAR data with an analysis of the differences between pre- and post-event images. The model is validated using cross-validation, in addition to a spatial validation using Sentinel2 images for one of the events, and a temporal validation based on the correlation between rainfall volume and flooded area along the events.

2. Methodology

2.1. Study Area

The Mar Menor is a coastal lagoon in south-eastern Spain (Figure 1), bounded by a 22 km long sand barrier. It is the largest coastal lagoon in the western Mediterranean. It is characterized by the fact that it has been recognized as an Important Ecological Area of Outstanding Value (IEOV) by European legislation, which places it under strict protection measures. The study area is the catchment area of the Mar Menor. This basin, called Campo de Cartagena, has a surface area of 1275 km^2 and a slight slope of less than 10%.

The climatic conditions of the basin are typically Mediterranean semi-arid, with irregular and scarce rainfall, usually below 300–350 mm/year, with a pronounced alternation of extreme droughts and floods due to the considerable spatial and temporal variability of rainfall. Rainfall is characterized by scarcity, with an annual mean of less than 300 mm in the plains. However, this low rainfall is episodic, often occurring in a few hours over a few days, and is insignificant over a nine-month period. As a result, the region enjoys more than 3000 h of sunshine per year, which means that temperatures are consistently warm throughout the year, with an average of 16 to 18 °C, depending on the proximity to the coast, and reaching maximum values of over 42 °C [90].

These climatic and orographic characteristics result in a scarcity of surface watercourses. The drainage network within the basin consists of a series of ephemeral basins that form during periods of heavy rainfall [90]. However, some of these basins drain mainly to the plain due to the lack of slope and eventually lead to flooding in the plain during periods of heavy rainfall.

However, the existence of favorable soil characteristics has led to the predominance of agriculture as the main economic driver since ancient times, gradually changing in the last half century from traditional rainfed crops to more profitable irrigated crops thanks to the arrival of water transferred from the Tagus River. According to the most recent regional statistics [91], there are almost 38,000 ha of irrigated grassland in addition to irrigated areas of dense tree crops on the lower slopes, and greenhouses cover more than 1500 ha. The second main use is urban. The urbanization of the municipalities bordering the lagoon and the construction of seasonal resorts, both tourist and second homes, are associated with an influx of tourist activity. However, the seasonal increase in the resident population is difficult to quantify. In terms of natural vegetation, there is a high level of biodiversity and heterogeneity of vegetation, mainly Mediterranean scrub, with some areas of Mediterranean forest.

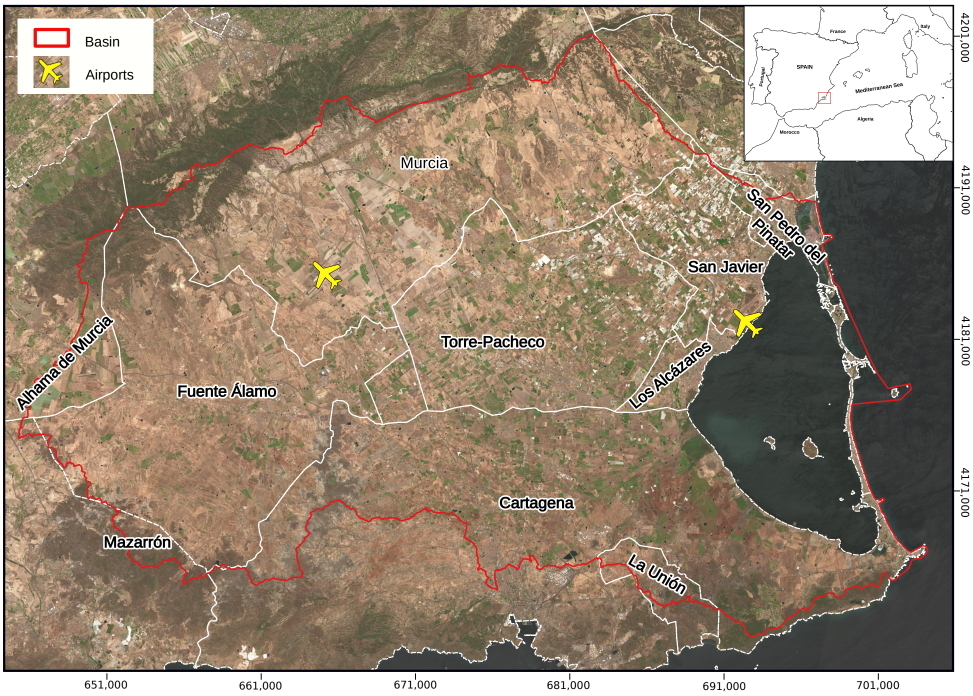

Figure 1. Study area including the location of airports and rain gauges used to calculate precipitation metrics. The coordinates refer to the ETRS89 datum and the UTM, Zone 30N, projection (EPSG: 25830).

All these factors have contributed to the significant economic importance of this area within the wider context of the Region of Murcia. Agricultural and residential development in the basin has been affecting the marine ecosystem for several decades [92,93]. In the Campo de Cartagena, intense urbanization is both a cause and an increase in the risk of flooding due to the imperviousness of the soil [94] and an increase in risk as more people and houses are exposed [95]. The impact of floods on human activities, the environment, and the economy is therefore considerable, as historical record shows. One of the most damaging events in recent decades, registered from 10 to 12 September 2019, was a torrential rainfall episode that led to an estimated economic loss of nearly 600 million euros, the loss of several human lives, and difficult to repair damage to the biodeversity of an invaluable ecosystem [96,97].

2.2. Data

All data were acquired from the Copernicus Data Space Ecosystem [98]. The images were obtained using the Terrain Observation by Progressive Scans SAR (TOPSAR) configuration at Level-1 Single Look Complex (SLC) in Interferometric mode (IW), the main acquisition mode of this sensor over the Earth's surface, with a full swath of 250 km and 5×20 m spatial resolution in a single look. TOPSAR steers the beam from backwards to forwards in the azimuth direction with an overlap to ensure continouos coverage. Level 1 SLC products contain backscater intensity and phase information that facilitates the discrimanation of pixel features from water and non-water. Data collection includes images from the same relative orbit, ensuring data from the same area at similar time periods in both ascending and descending directions, with azimuth angles ranging from 29.1 to 46°. Although backscatter is expected to vary with angle of incidence, especially when data collected in different orbital directions [99], the low slope that characterizes the area, the radiometric calibration and terrain correction processes applied in pre-processing, and the use of water training areas instead of thresholding are sufficient to make these variations not problematic.

The data used in this study (Table 1) were the intensity bands in co- (VV) and cross-polarization (VH) of the Sentinel 1 SAR imagery Ground Range Detected (GRD) product. The GRD product is focused, multi-looked, projected to ground range, composed of all burst and sub-swaths merged, and resampled to the common pixel spacing.

Table 1. Nomenclature of images used to analyze each event. Note that S1B data were not available from the end of 2021 due to a system malfunction, so only S1A data were used from then on.

Event	Images S1A	Images S1B
1	S1A_IW_GRDH_1SDV_20161124T061008_20161124T061033_014080_016B63_DABC S1A_IW_GRDH_1SDV_20161124T061008_20161124T061033_014080_016B63_DABC S1A_IW_GRDH_1SDV_20161206T061007_20161206T061032_014255_0170E4_37C1 S1A_IW_GRDH_1SDV_20161206T061032_20161206T061057_014255_0170E4_B0B3 S1A_IW_GRDH_1SDV_20161218T061007_20161218T061032_014430_017666_2AF7 S1A_IW_GRDH_1SDV_20161218T061032_20161218T061057_014430_017666_CA83	S1B_IW_GRDH_1SDV_20161224T060925_20161224T060950_003534_0060AE_C881
2	S1A_IW_GRDH_1SDV_20170111T061005_20170111T061030_014780_01811D_9DA1 S1A_IW_GRDH_1SDV_20170111T061030_20170111T061055_014780_01811D_E66E S1A_IW_GRDH_1SDV_20170123T061005_20170123T061030_014955_018698_AE68 S1A_IW_GRDH_1SDV_20170123T061030_20170123T061055_014955_018698_1FBC	S1B_IW_GRDH_1SDV_20170117T060923_20170117T060948_003884_006B01_CCA8
3	S1A_IW_GRDH_1SDV_20170827T061008_20170827T061033_018105_01E680_CC5A S1A_IW_GRDH_1SDV_20170827T061033_20170827T061058_018105_01E680_8DAE	S1B_IW_GRDH_1SDV_20170821T060945_20170821T061010_007034_00C646_C9A9 S1B_IW_GRDH_1SDV_20170902T060945_20170902T061010_007209_00CB57_12A7
4	S1A_IW_GRDH_1SDV_20180118T061007_20180118T061032_020205_022790_28AD S1A_IW_GRDH_1SDV_20180118T061032_20180118T061057_020205_022790_0687 S1A_IW_GRDH_1SDV_20180130T061006_20180130T061031_020380_022D20_124A S1A_IW_GRDH_1SDV_20180130T061031_20180130T061056_020380_022D20_C24E	S1B_IW_GRDH_1SDV_20180124T060944_20180124T061009_009309_010B3B_A34D
5	S1A_IW_GRDH_1SDV_20180506T061008_20180506T061033_021780_025963_F8C4 S1A_IW_GRDH_1SDV_20180506T061033_20180506T061058_021780_025963_AB5D	S1B_IW_GRDH_1SDV_20180430T060945_20180430T061010_010709_0138F2_C906 S1B_IW_GRDH_1SDV_20180512T060946_20180512T061011_010884_013E97_6108
6	S1A_IW_GRDH_1SDV_20180518T061009_20180518T061034_021955_025EF3_CB2A S1A_IW_GRDH_1SDV_20180518T061034_20180518T061059_021955_025EF3_85A8 S1A_IW_GRDH_1SDV_20180530T061009_20180530T061034_022130_026493_4F1B S1A_IW_GRDH_1SDV_20180530T061034_20180530T061059_022130_026493_C1EE	S1B_IW_GRDH_1SDV_20180524T060946_20180524T061011_011059_014449_A2C7 S1B_IW_GRDH_1SDV_20180605T060947_20180605T061012_011234_0149EC_FF2D
7	S1A_IW_GRDH_1SDV_20180903T061015_20180903T061040_023530_028FEB_799C S1A_IW_GRDH_1SDV_20180903T061040_20180903T061105_023530_028FEB_ECF4 S1A_IW_GRDH_1SDV_20180915T061015_20180915T061040_023705_029586_A4EA S1A_IW_GRDH_1SDV_20180915T061040_20180915T061105_023705_029586_0057	S1B_IW_GRDH_1SDV_20180828T060952_20180828T061017_012459_016F9A_6935 S1B_IW_GRDH_1SDV_20180909T060953_20180909T061018_012634_017500_5662 S1B_IW_GRDH_1SDV_20180921T060953_20180921T061018_012809_017A59_B633
7	S1A_IW_GRDH_1SDV_20181114T061016_20181114T061041_024580_02B2D5_5589 S1A_IW_GRDH_1SDV_20181114T061041_20181114T061106_024580_02B2D5_EE00	S1B_IW_GRDH_1SDV_20181003T060953_20181003T061018_012984_017FB6_0281 S1B_IW_GRDH_1SDV_20181108T060953_20181108T061018_013509_018FF3_AD05 S1B_IW_GRDH_1SDV_20181120T060953_20181120T061018_013684_019579_7E62
9	S1A_IW_GRDH_1SDV_20190407T061013_20190407T061038_026680_02FE88_359D S1A_IW_GRDH_1SDV_20190407T061038_20190407T061103_026680_02FE88_34E6 S1A_IW_GRDH_1SDV_20190419T061013_20190419T061038_026855_0304E2_5040 S1A_IW_GRDH_1SDV_20190419T061038_20190419T061103_026855_0304E2_9FB5	S1B_IW_GRDH_1SDV_20190413T060951_20190413T061016_015784_01DA0A_1C2E S1B_IW_GRDH_1SDV_20190425T060951_20190425T061016_015959_01DFD4_B029
10	S1A_IW_GRDH_1SDV_20190910T061021_20190910T061046_028955_034891_EDAB S1A_IW_GRDH_1SDV_20190910T061046_20190910T061111_028955_034891_D799 S1A_IW_GRDH_1SDV_20190916T180159_20190916T180224_029050_034BE2_3693 S1A_IW_GRDH_1SDV_20190916T180224_20190916T180249_029050_034BE2_F390	S1B_IW_GRDH_1SDV_20190904T060959_20190904T061024_017884_021A81_9492
11	S1A_IW_GRDH_1SDV_20191121T061022_20191121T061047_030005_036CD8_C962 S1A_IW_GRDH_1SDV_20191121T061047_20191121T061112_030005_036CD8_D8B5 S1A_IW_GRDH_1SDV_20191203T061021_20191203T061046_030180_0372EA_EB2D S1A_IW_GRDH_1SDV_20191203T061046_20191203T061111_030180_0372EA_EA7B	S1B_IW_GRDH_1SDV_20191127T060959_20191127T061024_019109_024106_5C20 S1B_IW_GRDH_1SDV_20191209T060959_20191209T061024_019284_02468F_3DE6
12	S1A_IW_GRDH_1SDV_20200114T180209_20200114T180234_030800_03886B_6543 S1A_IW_GRDH_1SDV_20200126T180208_20200126T180233_030975_038E95_75DB	S1B_IW_GRDH_1SDV_20191221T060958_20191221T061023_019459_024C21_7934 S1B_IW_GRDH_1SDV_20200120T180118_20200120T180143_019904_025A67_3AEA S1B_IW_GRDH_1SDV_20200120T180143_20200120T180208_019904_025A67_0A0D
13	S1A_IW_GRDH_1SDV_20200314T180208_20200314T180233_031675_03A6D3_461A S1A_IW_GRDH_1SDV_20200326T180208_20200326T180233_031850_03ACFC_08DF S1A_IW_GRDH_1SDV_20200407T180208_20200407T180233_032025_03B327_FE7E	S1B_IW_GRDH_1SDV_20200320T180118_20200320T180143_020779_02766F_D3C8 S1B_IW_GRDH_1SDV_20200320T180143_20200320T180208_020779_02766F_7126 S1B_IW_GRDH_1SDV_20200401T180118_20200401T180143_020954_027BF7_C274 S1B_IW_GRDH_1SDV_20200401T180143_20200401T180208_020954_027BF7_AF41
14	S1A_IW_GRDH_1SDV_20201227T180216_20201227T180241_035875_043370_8BB4 S1A_IW_GRDH_1SDV_20210108T180215_20210108T180240_036050_043984_D6D1	S1B_IW_GRDH_1SDV_20210102T180125_20210102T180150_024979_02F915_487F S1B_IW_GRDH_1SDV_20210102T180150_20210102T180215_024979_02F915_E8E3 S1B_IW_GRDH_1SDV_20210114T180125_20210114T180150_025154_02FEB3_C368 S1B_IW_GRDH_1SDV_20210114T180150_20210114T180215_025154_02FEB3_1C3D
15	S1A_IW_GRDH_1SDV_20210225T180214_20210225T180239_036750_0451E1_B229 S1A_IW_GRDH_1SDV_20210309T180214_20210309T180239_036925_0457FF_DAB6	S1B_IW_GRDH_1SDV_20210303T180123_20210303T180148_025854_031561_9DD0 S1B_IW_GRDH_1SDV_20210303T180148_20210303T180213_025854_031561_413C S1B_IW_GRDH_1SDV_20210315T180123_20210315T180148_026029_031B0C_8AF2 S1B_IW_GRDH_1SDV_20210315T180148_20210315T180213_026029_031B0C_B917
16	S1A_IW_GRDH_1SDV_20210402T180214_20210402T180239_037275_046426_6E19 S1A_IW_GRDH_1SDV_20210414T180214_20210414T180239_037450_046A34_6D58 S1A_IW_GRDH_1SDV_20210426T180215_20210426T180240_037625_04703C_0C1D	S1B_IW_GRDH_1SDV_20210327T180124_20210327T180149_026204_03209B_E1CC S1B_IW_GRDH_1SDV_20210327T180149_20210327T180214_026204_03209B_4CE6 S1B_IW_GRDH_1SDV_20210408T180124_20210408T180149_026379_032624_B065 S1B_IW_GRDH_1SDV_20210408T180149_20210408T180214_026379_032624_4D64 S1B_IW_GRDH_1SDV_20210420T180125_20210420T180150_026554_032BC7_B070 S1B_IW_GRDH_1SDV_20210420T180150_20210420T180215_026554_032BC7_42BB S1B_IW_GRDH_1SDV_20210502T180125_20210502T180150_026729_033160_AEC5 S1B_IW_GRDH_1SDV_20210502T180150_20210502T180215_026729_033160_3792
17	S1A_IW_GRDH_1SDV_20210520T180216_20210520T180241_037975_047B69_58A3	S1B_IW_GRDH_1SDV_20210514T180126_20210514T180151_026904_0336D6_D9F3 S1B_IW_GRDH_1SDV_20210514T180151_20210514T180216_026904_0336D6_80F5 S1B_IW_GRDH_1SDV_20210526T180126_20210526T180151_027079_033C2F_3EDB S1B_IW_GRDH_1SDV_20210526T180151_20210526T180216_027079_033C2F_19C8
18	S1A_IW_GRDH_1SDV_20220214T061030_20220214T061055_041905_04FD4E_6B2E S1A_IW_GRDH_1SDV_20220214T061055_20220214T061120_041905_04FD4E_F6EB S1A_IW_GRDH_1SDV_20220220T180219_20220220T180244_042000_0500A2_3CF0 S1A_IW_GRDH_1SDV_20220226T061030_20220226T061055_042080_050355_6088 S1A_IW_GRDH_1SDV_20220226T061055_20220226T061120_042080_050355_B606 S1A_IW_GRDH_1SDV_20220304T180219_20220304T180244_042175_050694_B224 S1A_IW_GRDH_1SDV_20220310T061030_20220310T061055_042255_050941_03BA S1A_IW_GRDH_1SDV_20220310T061055_20220310T061120_042255_050941_8676 S1A_IW_GRDH_1SDV_20220316T180219_20220316T180244_042350_050C8C_F393 S1A_IW_GRDH_1SDV_20220322T061031_20220322T061056_042430_050F38_EA76 S1A_IW_GRDH_1SDV_20220322T061056_20220322T061121_042430_050F38_2BDD S1A_IW_GRDH_1SDV_20220328T180220_20220328T180245_042525_05127F_A171 S1A_IW_GRDH_1SDV_20220403T061031_20220403T061056_042605_051528_75D1 S1A_IW_GRDH_1SDV_20220403T061056_20220403T061121_042605_051528_1418	
19	S1A_IW_GRDH_1SDV_20220924T180229_20220924T180254_045150_056567_4E1C S1A_IW_GRDH_1SDV_20220930T061040_20220930T061105_045230_056802_42A6 S1A_IW_GRDH_1SDV_20220930T061105_20220930T061130_045230_056802_6199 S1A_IW_GRDH_1SDV_20221006T180229_20221006T180254_045325_056B40_4506 S1A_IW_GRDH_1SDV_20221012T061040_20221012T061105_045405_056DEA_C6B7 S1A_IW_GRDH_1SDV_20221012T061105_20221012T061130_045405_056DEA_9C11	

The pre-processing workflow [100] was carried out in the Sentinel Application Platform (SNAP) software (version 8), which included a slice assembly where necessary prior to a subset in the study area and as recommended by [100] to pre-process the S1 imagery to address potential geometric issues, including a radiometric calibration step, a speckle filtering procedure using a 5 × 5 window Lee sigma filter with a sigma of 0.9 and a target size of 3 × 3, and a terrain correction with resampling to 10 m using the nearest neighbor model to the SRTM 1Sec HGT digital elevation model. Finally, the data were converted to dB.

Table 2 shows the rainfall events to be analyzed. For each event, two images before the event and all images until the first after the event were used. The two previous images were used to characterize the water and non-water areas in terms of the metrics used, but also to analyze the distribution of changes between two close images before the event.

In addition to VV and VH, four metrics (VVVH, VV/VH, VV+VH and VV-VH) were calculated. We did not use VV^2 or VH^2 as in [44] because the square, as a monotonically increasing function, does not add any new information to thresholding or decision trees.

Table 2. Analyzed events. Average precipitation (mm) in the study area, value registered in the weather station with maximum rainfall (mm) and duration (hours).

Event	Initial Date	Final Date	Mean Rainfall	Max Rainfall	Duration
1	04/12/2016:09	20/12/2016:00	210.6	316.0	15.62
2	19/01/2017:08	19/01/2017:21	58.4	84.2	0.54
3	29/08/2017:10	30/08/2017:14	30.4	44.2	1.17
4	27/01/2018:22	28/01/2018:16	30.3	46.27	0.75
5	09/05/2018:11	10/05/2018:21	7.7	35.75	1.42
6	29/05/2018:09	03/06/2018:03	12.1	32.8	4.75
7	08/09/2018:05	15/09/2018:16	35.6	61.2	6.46
8	14/11/2018:19	19/11/2018:12	92.7	135.6	4.71
9	19/04/2019:00	22/04/2019:21	101.7	132.4	3.87
10	10/09/2019:15	12/09/2019:20	195.2	283.7	2.21
11	01/12/2019:22	04/12/2019:08	65.6	157.5	2.41
12	19/01/2020:00	22/01/2020:11	81.4	110.3	3.46
13	21/03/2020:00	04/04/2020:23	144.9	186.8	14.96
14	04/01/2021:00	12/01/2021:23	43.7	72.3	8.96
15	05/03/2021:00	12/03/2021:23	54.7	80.6	7.96
16	06/04/2021:00	28/04/2021:23	51.9	85.6	22.96
17	22/05/2021:00	25/05/2021:23	57.6	79.2	3.96
18	23/02/2022:00	28/03/2022:23	165	231.9	5.96
19	04/10/2022:00	11/10/2022:23	32.4	118.8	7.96

2.3. Algorithms

2.3.1. Thresholding

Global thresholding is difficult in this case because there are no natural water bodies in the study area other than the sea. Both the Mediterranean Sea and the Mar Menor could be used to obtain water training data, but waves in response to stormy weather can be large enough to introduce excessive noise. Campo de Cartagena has many irrigation ponds that are calm enough to be used as water bodies. However, the area occupied by these ponds is very small, so the histograms obtained are not bimodal, making it difficult to obtain a suitable threshold. Instead, we used these irrigation ponds as water training areas; the non-water training points were obtained from agricultural or natural vegetation pixels with a slope of less than 5 degrees. Analyzing the superposition of the distribution of the 6 analyzed SAR metrics in water and non-water training areas provides an error metric that can also be used to determine which metric provides better accuracy.

2.3.2. Random Forest Classification

One of the problems with thresholding is that each SAR metric has a different threshold and can give different results for the likelihood of flooding. To integrate the information contained in the 6 SAR metrics, a Random Forest model is calibrated using the training data and these metrics as predictors. Random Forest (RF) is a non-parametric classification-regression method proposed in [101] that outperforms other traditional methods. Its main advantages include the following: high capacity to handle large predictor data sets, high prediction accuracy, ability to produce a feature importance metric and an internal accuracy estimate without, in principle, needing external validation. Finally, it is very easy to calibrate and optimize because, unlike support vector machines or neural networks, it is very insensitive to the values of its hyperparameters.

It is based on an ensemble of unpruned decision trees, 500 being the default number, calibrated with subsets of the training data generated by bootstrapping. In addition, for each node split of each tree, instead of selecting the feature that increases homogeneity from the full set of predictors, a random subset is used. In classification problems, the size of this subset is, by default, the square root of the number of predictors. These somewhat counterintuitive decisions reduce the correlation between the trees, increasing their variance and reducing the bias of their average. The feature importance metric is calculated by calculating how the accuracy changes when an individual variable is included or excluded from the subsets.

After calibration, any new case can be predicted by all the trees and the most frequent result is taken as the final estimate of the model. However, it is also possible to obtain the proportion of trees that produced each outcome. In binomial classification (water or non-water), this means obtaining the probability of water being present according to the model.

2.3.3. Detection of Permanent Water Bodies and Infrastructures

Irrigation ponds are obviously detected as flooded areas when they are not; the case is similar with the two airports (Figure 1) in the study area and several golf courses. These are very flat and smooth surfaces that respond to radar in a similar way to water. In order to filter out these land covers, a layer with the average water probability according to RF along the 19 events and another with the standard deviation along all processed images are calculated. The results contain three types of cells: 1. Cells with low average probability and low standard deviation, corresponding to areas that are never flooded; 2. Cells with high average probability and low standard deviation, corresponding to flat infrastructures and irrigation pods; 3. Finally, cells with intermediate average and high standard deviation, corresponding to areas that only appear flooded in some images.

2.3.4. Change Detection

Another approach to locating flooded areas is to calculate the difference between the SAR metrics before and after the rain event. The larger the difference in absolute value, the more likely it is that the cell is flooded; however, it is necessary to account for variability in the differences measured in non-flooded cells. In order to take this variability into account, the difference between two layers before the rainfall event was obtained and the empirical probability distribution was calculated. Such a distribution could then be used to calculate the probability of a difference greater than or equal to the measured difference between the metrics before and after the event, assuming no flooding occurred. We converted this p-value into a probability of flooding as

$$P_1(flooded) = max(0, -2 * (p - val - 0.5)) \quad (1)$$

If the p-value is 0, the resulting probability is 1, and if the p-value is 0.5 or greater, the probability is 0. This equation is used for VV, VH, and VV+VH. For VVVH, the minus sign in -2 is omitted because in this case the largest values are those representing water.

The probability maps produced by RF make it possible to apply change detection using two different approaches:

1. Calculate the increase in probability from an image previous to the event as $(P - P_0)/(1 - P_0)$ where P is the probability of water presence after the event and P_0 is the probability of water presence before the event.
2. Compute the difference in probability of water presence in two consecutive images before the event, compute the empirical distribution function of the differences (EDFp), and compute the p-value of the probability difference before and after the event for each pixel in the study area.

In the rest of the paper, the probability of water presence according the RF model is called just RF, the approach based on the increase in probability is called RFinc, and the approach based on the EDF of differences is called RFdif.

2.3.5. Slope Correction

Due to shadow effects in higher areas, it is necessary to filter out cells with large slopes. In this case, we obtained another possibility of flood presence because of the slope as

$$P_2(flooded) = max\left(\frac{5 - s}{5}, 0\right) \quad (2)$$

For the final maps, the probability of flooding is calculated as the minimum of both the model probability and the slope possibility. This is equivalent to an AND operator in fuzzy logic.

2.4. Validation

Validation in flooded area detection poses several issues. The usual approach would be to manually digitize flooded and non-flooded polygons as test areas from optic images of a close date. However, usually, it is not possible to find a cloud-free adequate image at the end of the rainfall event. Even a few days worth of delay between the two images (S1 and S2) might mean the loss of most of the water due to soil infiltration or evaporation. As it is a small slope area, evaporation can be considered to be the same in all the study area. Infiltration, on the contrary, has important variations due to different soil properties and previous water content.

In this study, only one image was found close enough in time to the rainfall event and with a cloud percentage low enough to allow the digitalization of the training areas. This is the image of 13 September 2019, three days before the SAR1 image classified (16 September 2019). Another MSI image (18 September 2019) shows that almost all water had disappeared by that day; Figure 2 shows a comparison between the two images. This means that a large proportion of water present in the 13 September 2019 MSI image could have been lost by 16 September 2019, when the SAR image was taken. A pixel-based validation, using the former image, of a model calibrated with the later could overestimate false negatives, as pixels dry in the later date could still be flooded in the former. Instead, we decided to perform polygon-based validation.

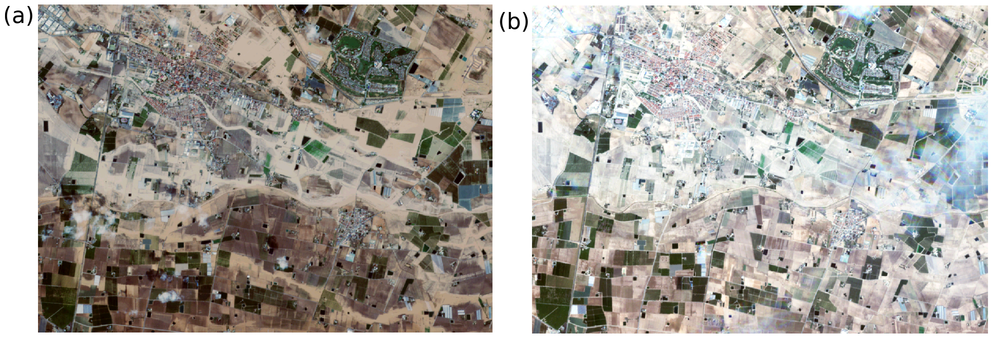

Figure 2. 13 September 2019 (**a**) and 18 September 2019 (**b**) MSI RGB compositions. Flooded areas are clearly visible in the first image, but they disappeared in a second.

Assuming that most flooded polygons lost water and had decreased in size from 13 September 2019 to 16 September 2019, we took into account only those pixels whose water probability is larger than the 0.9 percentile of the polygon and compute the median of those pixels. Plotting those values provides information of how well each of the methods separate flooded and non-flooded areas.

Due to the problems that using S2 images poses, another form of validation was attempted. It consisted in calculating the correlation among metrics extracted from the flooded probability maps (mean flood probability and flooded area) with two simple metrics extracted from the weather station data (average total rainfall and total rainfall in the station that registered the larger rainfall magnitude).

Figure 3 summarizes the employed methodology.

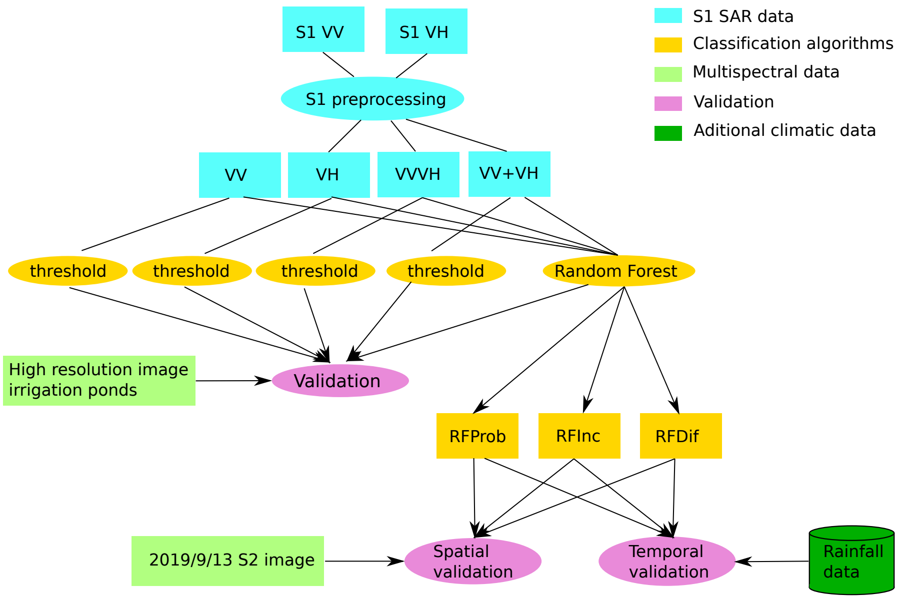

Figure 3. Methodological graphical summary.

3. Results

3.1. Thresholding

Figure 4 shows the distribution of the values of the analyzed metrics for both water and no water cells in the study area on 6 December 2016. Obviously, the more separated the distributions, the more accurate the classification based on a threshold. The error classification error can be calculated as (AUWd + AUNd)/(AUW + AUN), where AUW is the area under the distribution of water cells, AUN is the area under the distribution of no water cells. AUWd is the area under the distribution of water cells for values above the threshold and AUNd is the area under the distribution of no water cells for values below the threshold. It seems that at least in this case, the accuracy of VV is higher than that of VH. VV+H and VVVH have even better accuracies, while VV-VH and VV/VH have rather lower accuracies.

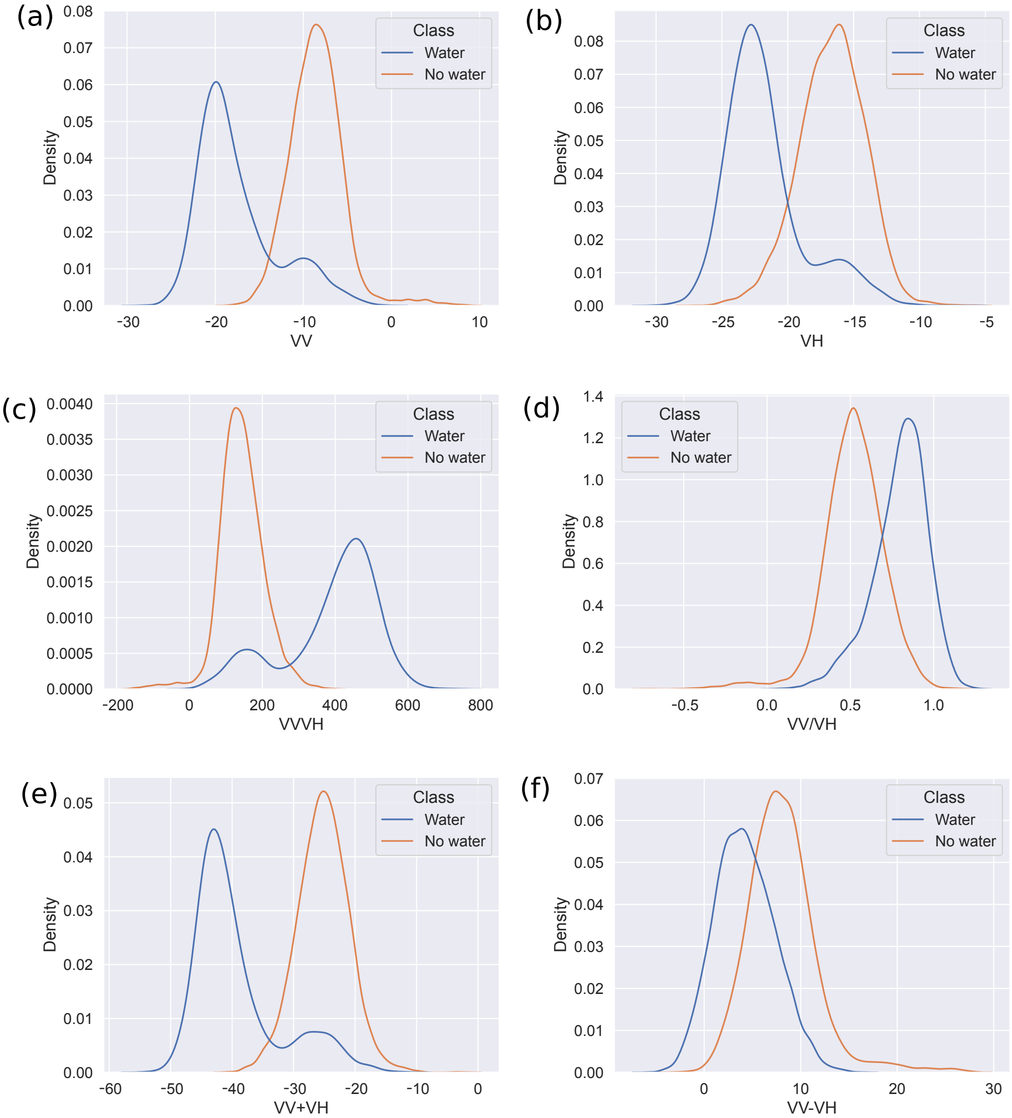

Figure 4. Value distribution of the used predictors: VV (**a**), VH (**b**), VVVH (**c**), VV/VH (**d**), VV+VH (**e**) and VV-VH (**f**) for water and non-water cells on 6 December 2016.

3.2. Classification

Figure 5 shows the distribution of the classification error along the different data points based on the thresholds of each feature. The error for VV is much lower than for VH. Two of the features created (VVVH and VV+VH) show even smaller errors, while VV-VH and VV/VH show larger errors. Table 3 shows the summary statistics of both the errors and the thresholds. It is clear that VV, VVVH, and VV+VH are the best metrics for distinguishing water cells from non-water cells.

After using Random Forest to classify water and non-water cells in all the images analyzed, we computed an accuracy whose distribution is shown in Figure 6. This figure also shows the distribution of the variable importance for each SAR metric. The results are consistent with those shown in Figure 5; the most relevant features to discriminate water cells from non-water cells according to the Random Forest algorithm are VV, VV+VH, and VVVH.

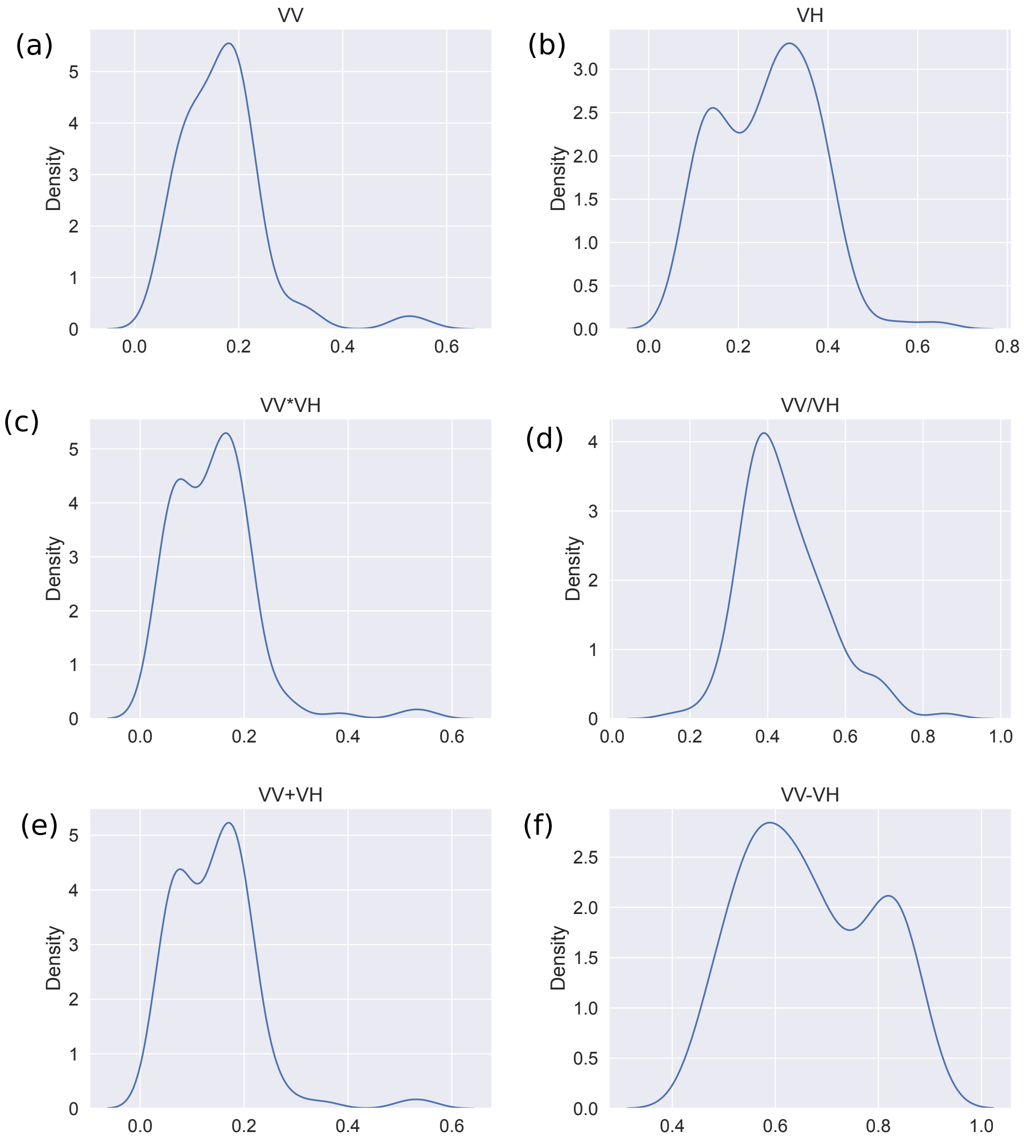

Figure 5. Distribution of classification error as proportion of overlapping among water and non-water distributions for all SAR metrics analysed: VV (**a**), VH (**b**), VVVH (**c**), VV/VH (**d**), VV+VH (**e**) and VV-VH (**f**).

Table 3. Summary statistics of thresholds and errors for the different metrics.

Predictor	Mean Error	Std Error	Mean Threshold	Std Threshold	Mean Accuracy
VV	0.169	0.083	−14.098	1.085	0.831
VH	0.263	0.109	−20.451	0.963	0.737
VVHV	0.140	0.081	444.224	42.669	0.86
VV/VH	0.443	0.109	0.788	0.061	0.557
VV+VH	0.142	0.080	−34.838	2.226	0.858
VV-VH	0.667	0.124	6.664	0.882	0.333

The accuracy of the Random Forest model for the different image events is quite higher than for the thresholding models. The mean accuracy is 0.941 (standard deviation = 0.048), so the mean error is 0.059. The mean f1 is 0.931 with a standard deviation of 0.066. It is important to remember that these metrics and those in Table 3 measure the ability of the model, Random Forest or thresholds, to identify irrigation ponds. We are aware that flooded areas may not have exactly the same signature as irrigation ponds. Additional validation tests are therefore needed. To determine whether they can identify flooded areas, we use validation data from MSI images.

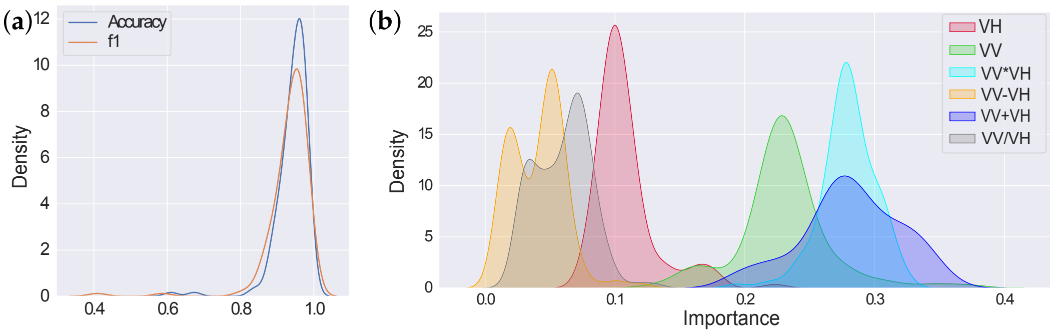

Figure 6. Results of RF classification of all the images. Accuracy distribution (**a**) and importance of the variables (**b**).

Figure 7 shows a heatmap showing the frequency of cells for different pairs of RF probability, mean, and standard deviation along all the images corresponding to the 19 analyzed events. One hundred bins were taken for each statistic, giving 10,000 possible bins. As expected, there are two extremes with low standard deviations, one with a high mean (infrastructure and irrigation ponds) and the other with a much higher frequency of cells that are always not flooded. The intermediate cells with high standard deviations correspond to cells that are temporarily flooded. As a result, an average probability threshold of 0.6 is set. Cells with a higher average are considered as infrastructure or irrigation ponds and are not counted as flooded.

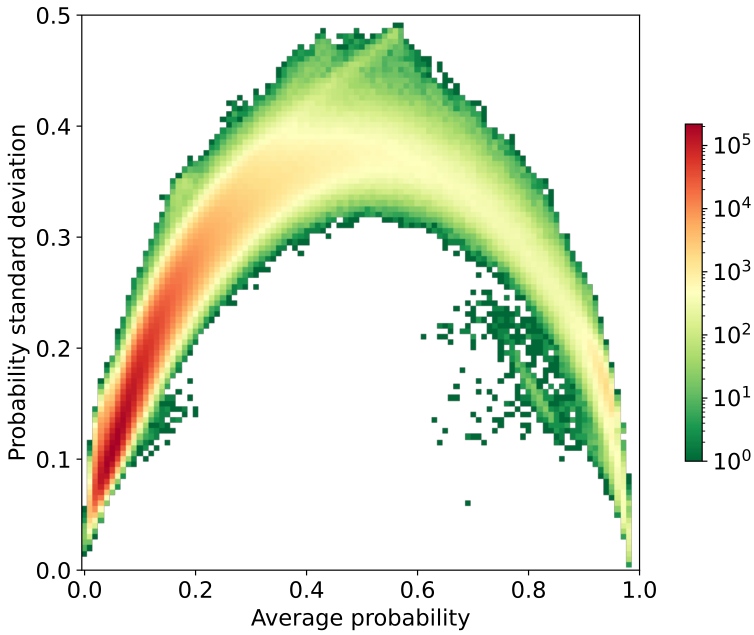

Figure 7. Heatmap with the cell frequency of different combinations of average probability and standard deviation of probability.

3.3. Differences

Figure 8 shows the distribution of the anomaly in the differences for the 5 June 2018 and 16 September 2019 S1 images for the four features identified as the most important features both in the Random Forest model and in the thresholding. Values close to zero reflect pixels where the difference between values in images after and before the event are not differerent from random variation, whereas values close to one reflect significant differences. Two facts might be highlighted. In the large precipitation event, the frequency of large values is higher than in the lower precipitation event. RFs produce quite lower significant variations than the other approaches. We think threshold-based methods are overestimating the flooded area, whereas RF gives a more accurate estimation. The pattern of low peaks for small values in RF is due to the approach of RF that delimits subspaces in the feature space and then average probabilities.

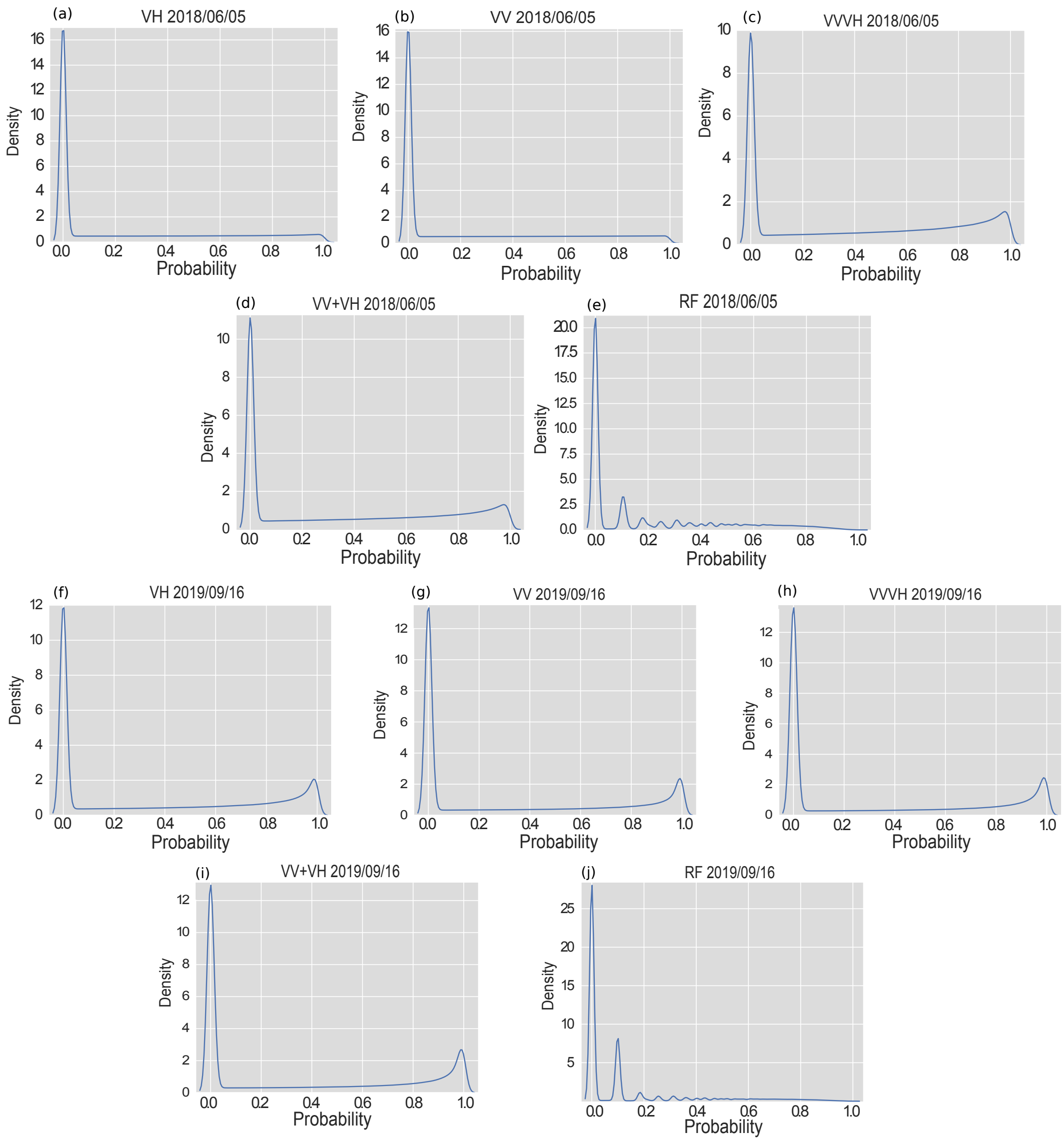

Figure 8. Difference anomalies of VH (**a**,**f**) , VV (**b**,**g**), VVVH (**c**,**h**), VV+VH (**d**,**i**), and RF (**e**,**j**) on the 5 June 2018 (**a**–**e**) and 16 September 2019 (**f**–**j**) S1 images.

Accuracy results are quite low considering that in a binomial classification, 0.5 is the accuracy to be expected from a random decision rule. The differences between the different methods are quite small, except for VV, whose accuracy is slightly lower than the other methods, and Random Forest, whose accuracy is slightly higher than the other methods. On the other hand, the thresholds chosen for the SAR metrics are surprisingly high, whereas the thresholds chosen for RF and RF increases are surprisingly low.

The problem with this validation attempt is that it is not clear whether the problem is related to the model being validated or to the difficulties of trying to validate flooded areas with a multispectral image taken 3 days before the SAR image used to calibrate the model. To check this issue, we assumed that most of the flooded areas present on 13 September 2019 (S1 date) would have decreased in size by 16 September 2019 (S2 date), so for each validation area, we took the cells with probability greater than the 0.9 quantile and calculated the median. Figure 9 shows the distribution of these medians. While the use of individual SAR metrics (VV, VVVH, and VV+VH) produces both false negatives and false positives, the methods based on RF classification produce only false negatives. Some of these false negatives could correspond to flooded areas that were present on 13 September 2019 and therefore registered as such in the validation data (S2), dried up by 16 September 2019 and therefore classified as not flooded using the S1 predictors. The result is an overestimation of the false negative rate.

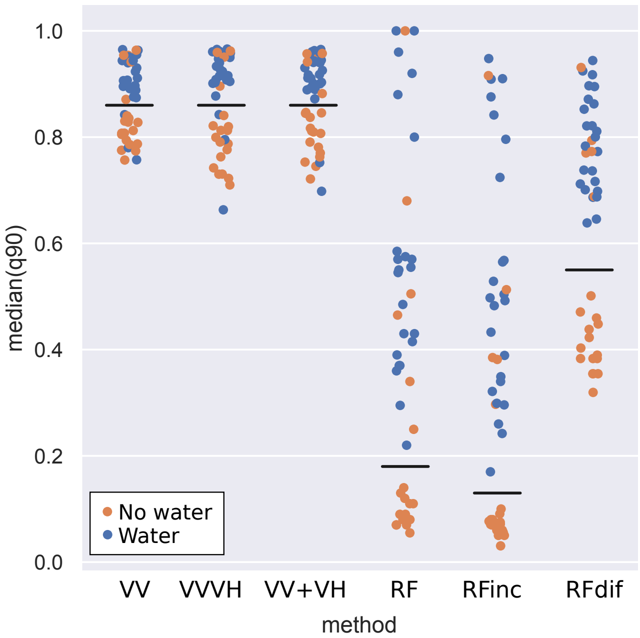

Figure 9. Distribution by class and method of the median probability of the polygon pixels with prob$>p_{90}$. Horizontal lines show the optimal threshold to separate the two classes for each method.

Table 4 shows the confusion matrices for the six methods and the corresponding accuracy statistics assuming the thresholds in Figure 9. Both Figure 9 and Table 5 show that the techniques derived from RF produce only false negatives, RF only one false positive and the rest of the methods produce more than one false positive. We believe that the aforementioned drying problem is the cause of the false negatives, whereas the false positives produced by VV, VVVH, and VV+VH are due to a lower predictive capacity.

Together with this validation, which we can call spatial and valid only for one episode, a temporal validation was carried out for all precipitation events. The first step was to calculate the correlation coefficients of five flood metrics focusing on the methods that did better in previous steps: Random Forest probability of flooding (RFprob), increase in RF probability (RFinc), RF flooded area (RFFA), increase in RF probability flooded area (RFIncFA), and RF difference in probability (RFDif) with two precipitation metrics: Total precipitation along the event averaged from different weather stations (Precipitaton) and Maximum precipitation measured in a single weather station. Table 6 shows the results.

Table 4. Polygon confusion matrices and accuracy statistics for the 6 methods analyzed.

	VV		VVVH		VV+VH		RFprob		RFinc		RFdif	
	N	W	N	W	N	W	N	W	N	W	N	W
N	15	5	15	5	15	5	14	6	15	5	15	5
W	3	21	3	21	2	22	1	23	0	24	0	24
accuracy	0.818		0.818		0.841		0.841		0.886		0.886	
kappa	0.63		0.63		0.675		0.672		0.766		0.766	

Table 5. Accuracy for a 0.5 probability threshold, Area Under the ROC Curve, optimized threshold according to the ROC curve, and accuracy using that threshold for the 6 methods tested: the three most accurate SAR metrics, Random Forest water probability, percentage increase in probability and probability difference.

Metric	Accuracy 0.5	AUC	Threshold	Accuracy Th
VV	0.569	0.56	0.86	0.6207
VVVH	0.599	0.59	0.834	0.632
VV+VH	0.596	0.594	0.815	0.633
RFprob	0.599	0.665	0.04	0.651
RFinc	0.597	0.598	0.091	0.642
RFdif	0.617	0.513	0.436	0.645

Table 6. Correlation between flood metrics and precipitation metrics. RFprob is the probability of water presence according to the Random Forest model, RFFA is the flooded area according to the model, RFinc is the increase in probability relative to the pre-event image, RFIncFA is the flooded area according to RFinc, and RFDif is the difference in probability relative to the pre-event image. The flooded area related to this last metric was not calculated due to its low performance.

	RFprob	RFFA	RFinc	RFIncFA	RFDif
Precipitation	−0.005	0.322	0.141	0.516	−0.053
Max. precipit.	0.067	0.371	0.234	0.572	−0.091

The two flooding metrics more highly correlated with the precipitation metrics are RFFA and RFIncFA, both related with the RF increase in probability method. Among them, the metric related with flooded area has the highest correlation. Figure 10 shows the relation of flooded area to precipitation and maximum precipitation. This figure also shows how the season of the year affects the resulting metric. Spring events seem to have less flooded areas whereas summer events have larger flooded areas. We think the reason is that summer events are mainly convective with large rainfall intensity in a few hours, whereas spring events are more related with frontal events with less intensity for the same amount of rainfall. In addition, in spring, vegetation has larger capacity to transpirate water and improve soil properties that favor water infiltration.

Finally, a RF model was fitted to evaluate the importance and the effects of these three predictors: precipitation, maximum precipitation, and season on flooded areas. The values of predictions were as follows: Total precipitation = 0.404, maximum precipitation = 0.334, winter = 0.027, spring = 0.132, summer = 0.057, fall = 0.0462. The most important predictor is total precipitation, followed by maximum precipitation, whereas season is less important. These results are clearly in accordance with Figure 10.

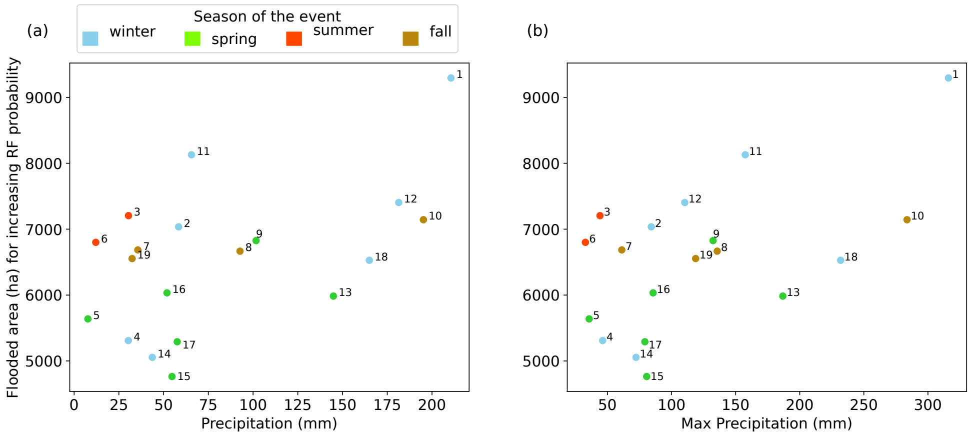

Figure 10. Flooded area in relation to precipitation (**a**) and maximum precipitation in a weather station (**b**). Numbering refers to Table 1 and colors reflect season.

The LOO-CV of the RF model to explain the area flooded from precipitation, maximum precipitation, and season shows a correlation coefficient of 0.451 and RMSE = 979 ha. It is clear that the fit is far from perfect and there are other factors that should be taken into account. Figure 11 shows the effects of the predictors on the model according to shapley procedure [102] implemented in the python shap package.

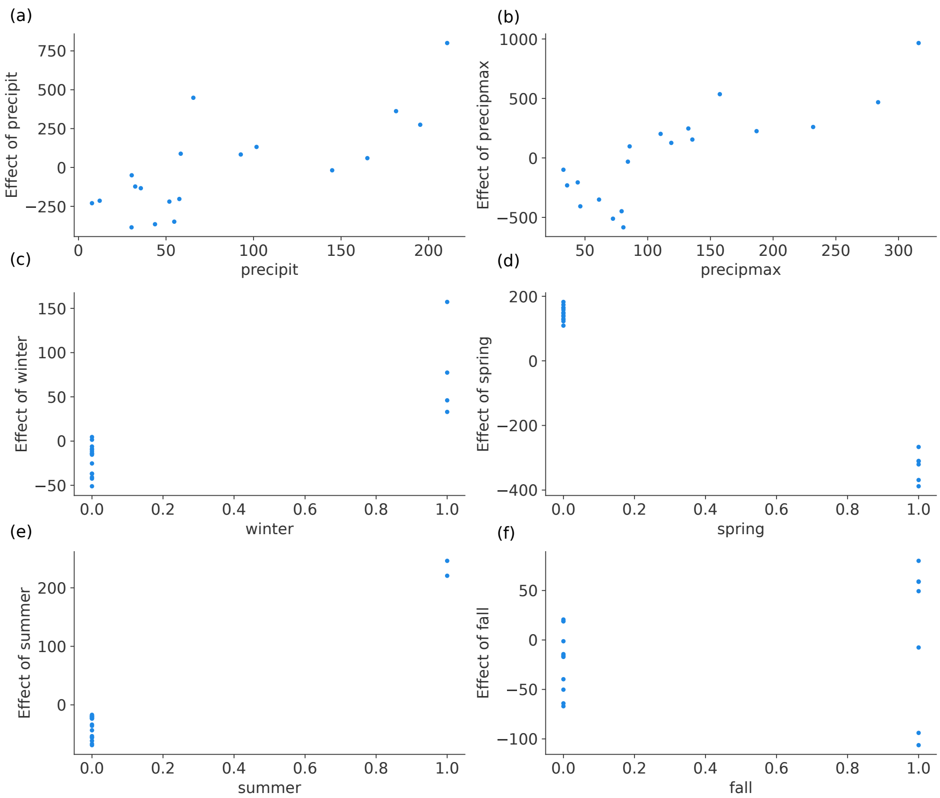

Figure 11. Effects of the RF model relating RFinc flooded area with precipitation and season metrics according to shap. (**a**) Effect of precipitation, (**b**) Effect of maximum precipitation, (**c**) Effect of winter, (**d**) Effect of spring, (**e**) Effect of summer, (**f**) Effect of fall.

The results show that the average precipitation on the study area and the precipitation in the weather station receiving more precipitation are good predictors of the surface flooded predicted by RF increased probability using S1 bands as predictors. Flooded area tends to increase in summer an decrease in spring, whereas in fall they retain average values. Winter shows a slight increase, but quite lower than in summer. This results corroborate those obtained in Figure 10.

Figures 12–15 show maps for RF flooding probability and increase in RF flooding probability in two events: 2018/05-06 is a low precipitation event, whereas 2019/09 is one of the largest precipitation events in the study area. The four figures show on the left the probability values and on the right the prediction of flooded and non-flooded areas. RF probability seems to overestimate flooded areas, whereas the increase in RF probability obtain a more reduced flooded area that better reflects the cycle of flooding and drying.

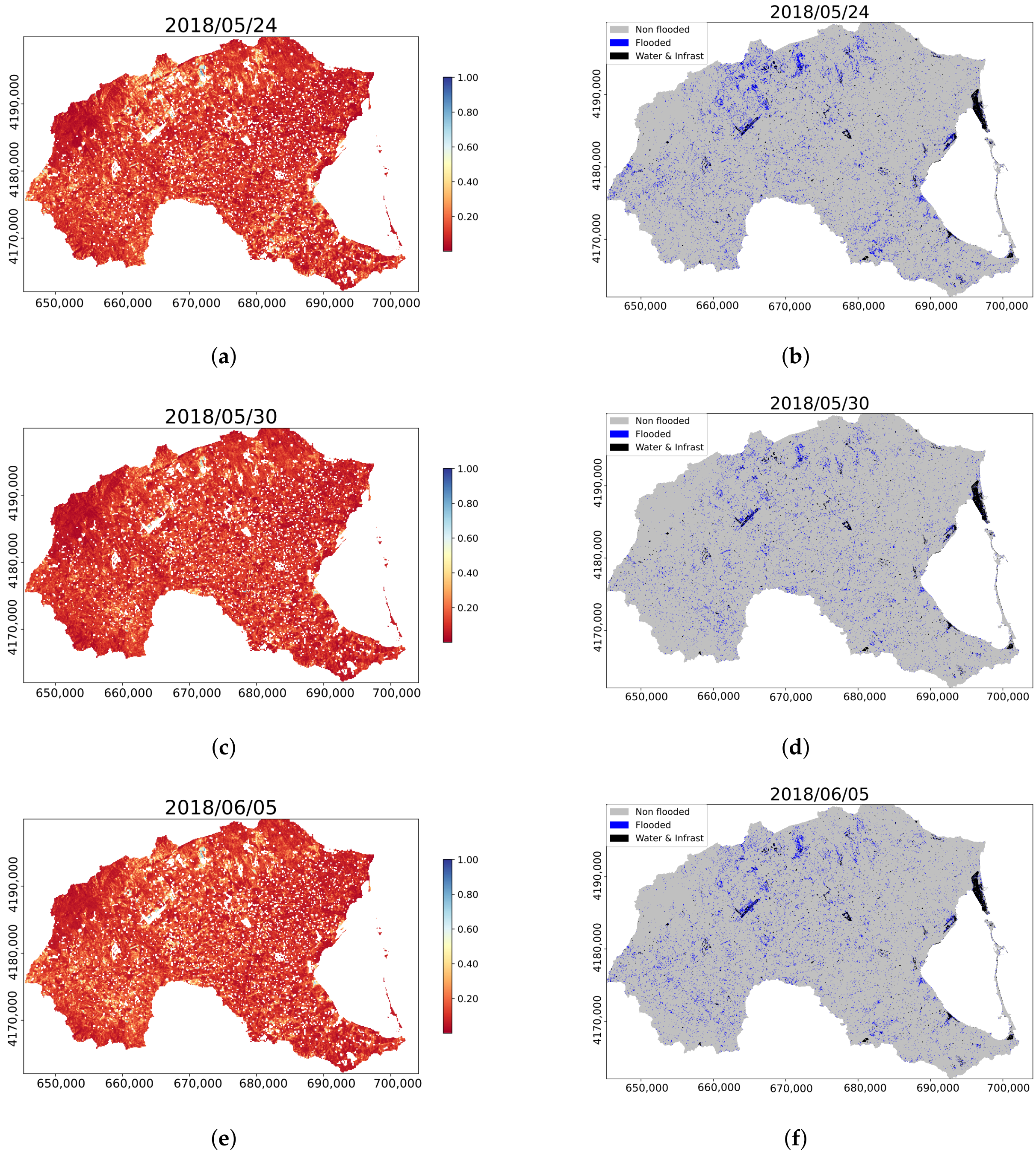

Figure 12. RF flooding probability (**a**,**c**,**e**) and final flooded area (**b**,**d**,**f**) in images from three consecutive dates in Event 6. The coordinates refer to the ETRS89 datum and the UTM, Zone 30N, projection (EPSG: 25830).

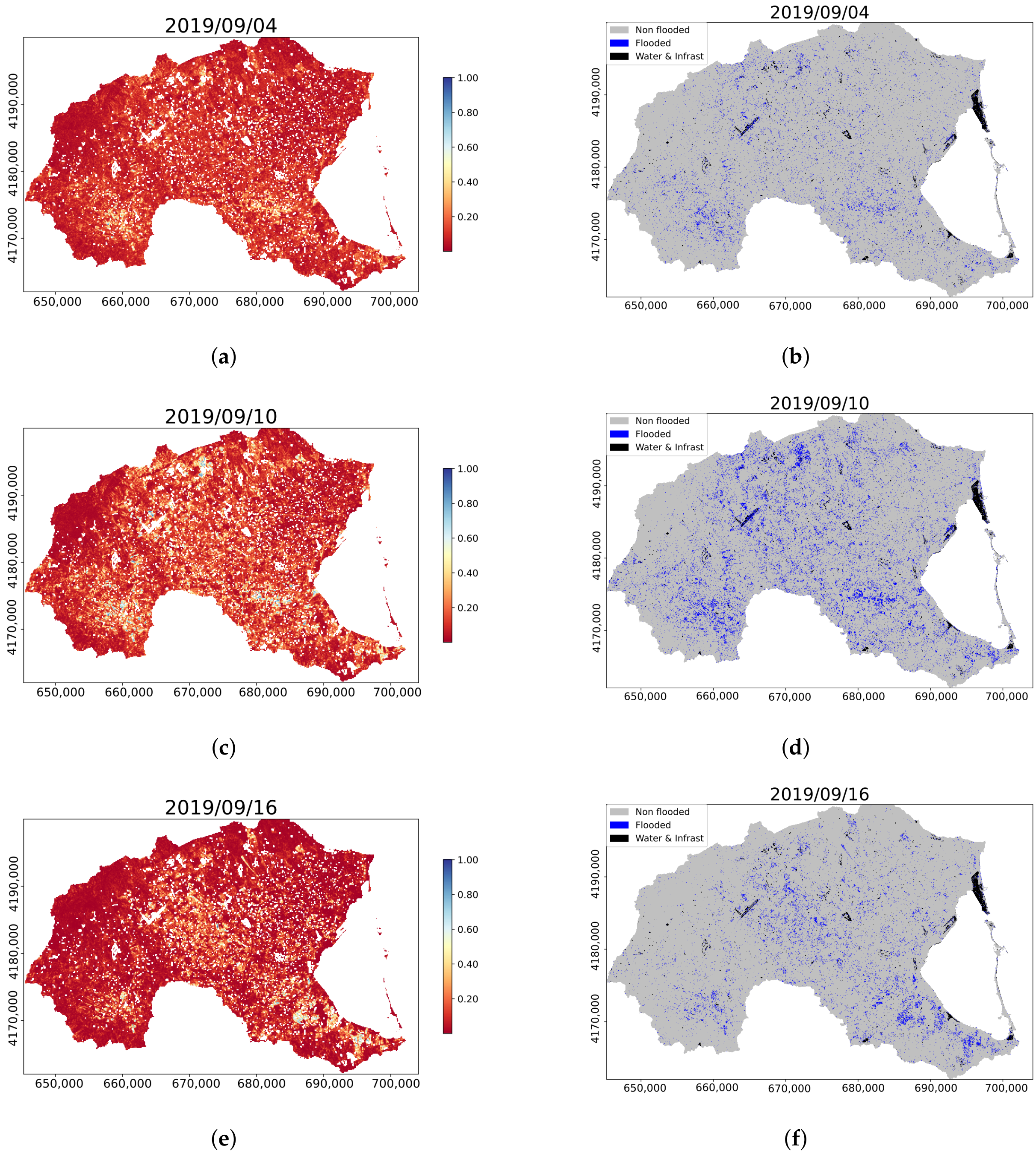

Figure 13. RF flooding probability (**a**,**c**,**e**) and final flooded area (**b**,**d**,**f**) in images from three consecutive dates in Event 10. The coordinates refer to the ETRS89 datum and the UTM, Zone 30N, projection (EPSG: 25830).

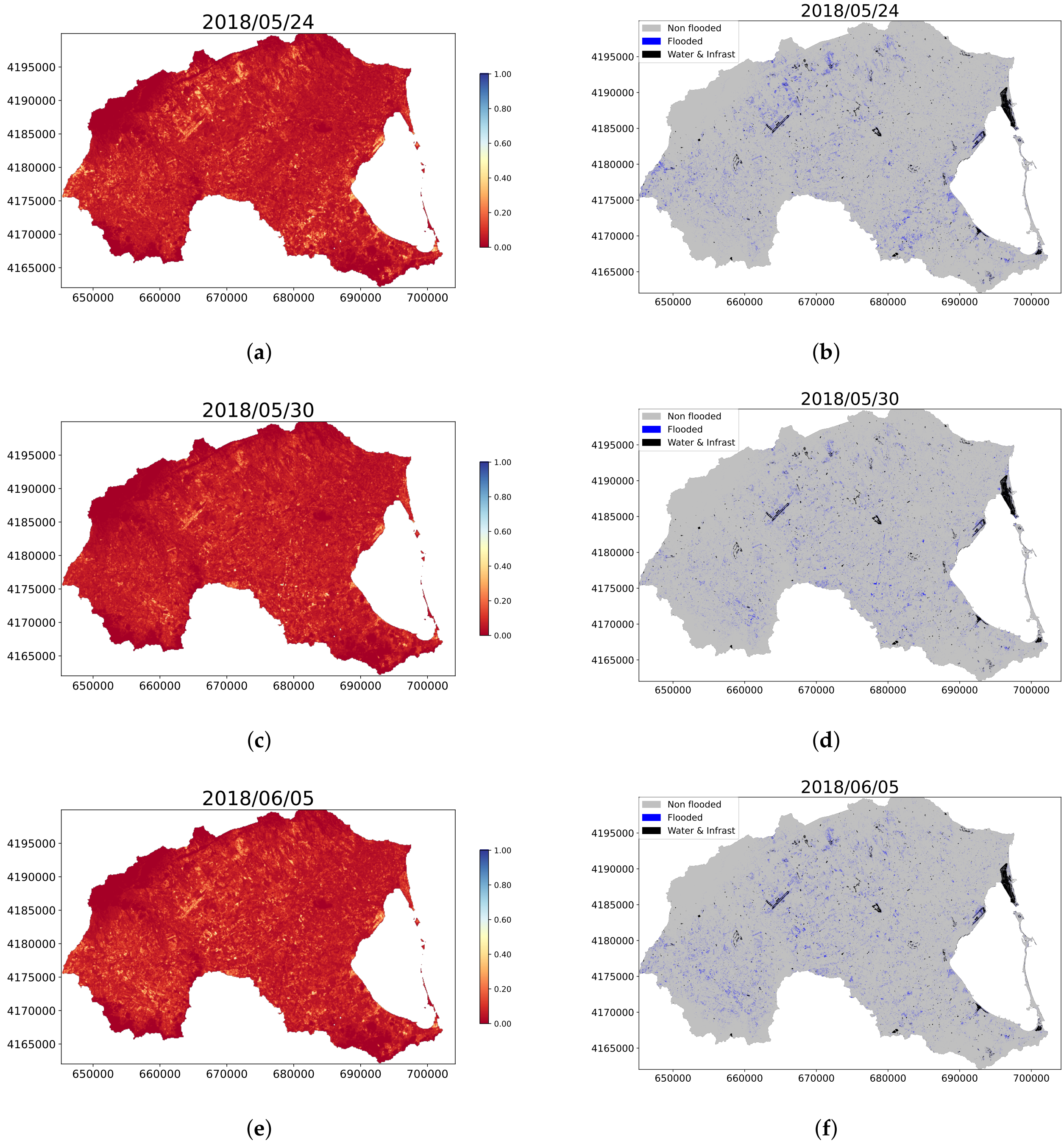

Figure 14. Increase in RF flooding probability (**a**,**c**,**e**) and final flooded area (**b**,**d**,**f**) in Event 6. The coordinates refer to the ETRS89 datum and the UTM, Zone 30N, projection (EPSG: 25830).

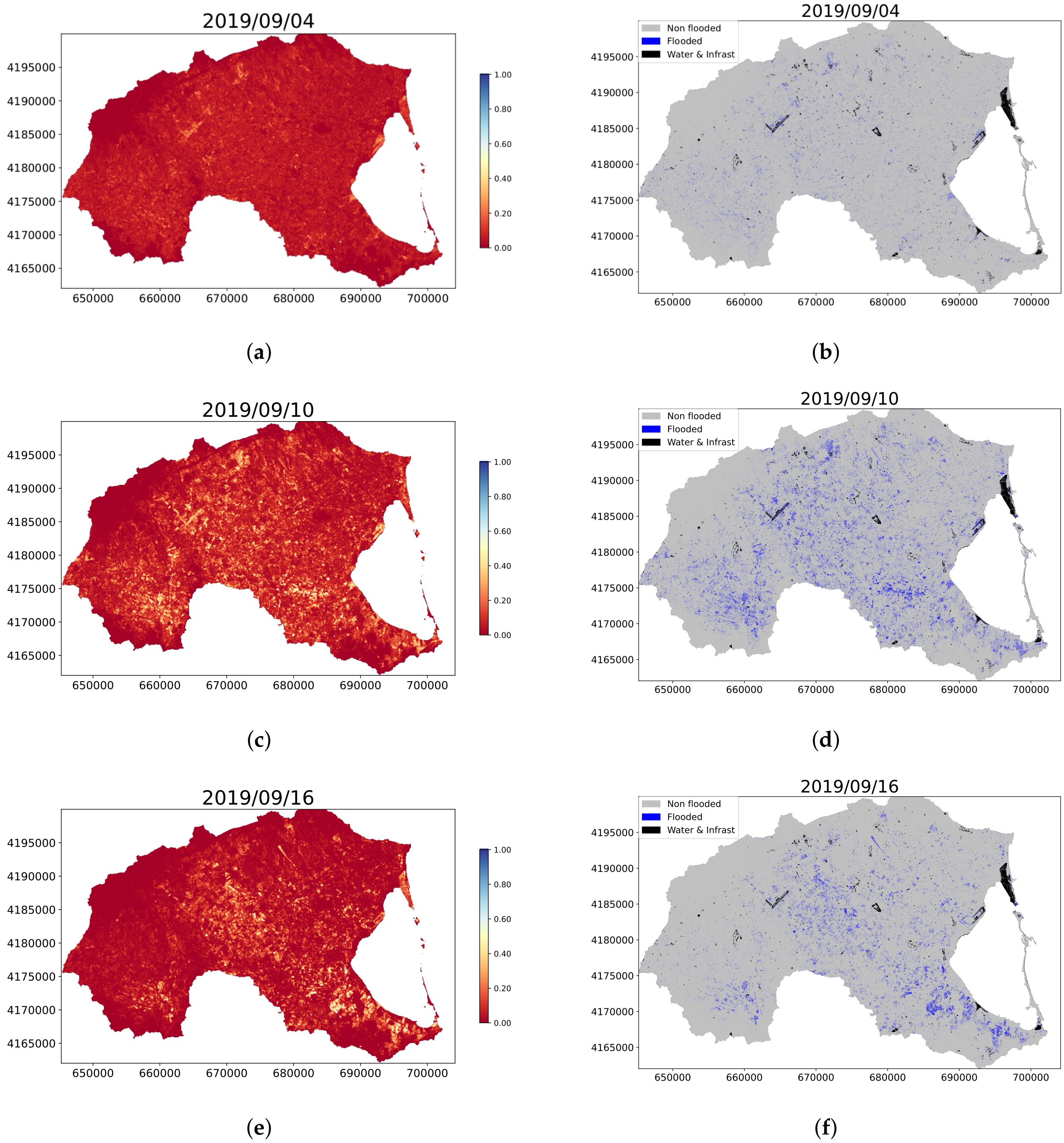

Figure 15. Increase in RF flooding probability (**a**,**c**,**e**) and final flooded area (**b**,**d**,**f**) in Event 10. The coordinates refer to the ETRS89 datum and the UTM, Zone 30N, projection (EPSG: 25830).

4. Discussion

Most of the work investigating the potential use of SAR data for water detection focuses on detecting changes in the extent of permanent water bodies. Such changes are not necessarily related to weather events but are monitored over the long term [28,34,61,64,72,103]. In these cases, it is easy to combine optical and radar data as in [72]; it is also easy to find calibration and validation cells from high-resolution optical images [103] or form the same SAR dataset that has been classified using the same water bodies whose extent is being monitored [28,61,64], and it is also easy to remove noise by excluding positive cells that are not in contact with the water bodies being analyzed using a region growing process [71]. In the case of this work, we were trying to detect flooded surface in a large study area with a low slope and with no natural water bodies. Cells taken from irrigation ponds were used as water calibration cells, and the expected output consists of water patches distributed all over the study area. The issue is that we assume that irrigation ponds respond to SAR in the same way as flooded areas. This is not an unreasonable assumption, as S1 image was taken 4 days after the event, so turbulence should be discarded, and both types of water surface are exposed to the same weather conditions, although the water depth in irrigation ponds is greater than in flooded areas. In any case, irrigation ponds would be a more extreme case of flooding, so the probabilities obtained from the classification could be biased towards lower values and produce false negatives. But it is difficult to check this without a map of flooded areas produced on the same day as the satellite image. This is an interesting line of research for the future.

Calibrating the model with irrigation ponds and validating with flooded areas has three advantages. First, the model can be calibrated using SAR data only, without the need for a multispectral image that could be affected by clouds. Second, we do not need to apply automatic thresholding, which could be difficult if most of the areas are not flooded. Third, the validation data are truly independent of the calibration data and could be extracted even from images half-covered by clouds.

The disadvantage is that the process of evaporation and infiltration of water over land is very rapid, especially in semi-arid areas. A clear day in late summer/early autumn after rainfall can evaporate a large amount of water. This is a very difficult challenge to validate if the two images are separated by even a few days. If the calibration image is taken after the validation image, as is the case in this study, we can expect an overestimation of false negatives, but not of false positives. If the order of the images were reversed, the opposite would be true.

Chen et al. (2020) obtain accuracies of 0.89 and 0.9 using thresholds with Envisat-WS and TerraSAR-X in China, respectively [103]. Gstaiger et al. (2012) obtain similar results with the same data and procedures in Vietnam [21]. Dong et al. (2021) and Luo et al. (2023) achieve accuracies better than 0.95 with different convolutional methods calibrated with Sentinel 1 data in China and Tibet, respectively [28,34]. The problem with convolutional methods is that they can have problems in correctly predicting the spatial boundaries of the classes, so if small flooded areas are expected, most of the flooded cells will be in the boundaries and convolutional networks will not perform well. To monitor flooded areas after extreme events, Li et al. (2019) use CNN with Terrasat-X and obtain overall accuracies between 0.9 and 0.93 in a study area near Houston [39]. Shen et al. (2019) achieve an accuracy of 0.93 in the Yangtze River and around Houston [13], and Liang and Liu (2020) with a threshold S1 of 0.99 in Louisiana around the Mississippi River [57]. In some cases, there is no explicit validation [29,64,69,103] and the authors give only a qualitative validation or produce a time series of estimated flooded areas.

In our study, the ability of the RF model to detect the water surface was demonstrated with a mean accuracy along all analyzed events of 0.941 (standard deviation=0.048) and a mean F1 of 0.931 with standard deviation=0.066. These values are in line with those obtained in other studies. However, an attempt to validate using optical imagery (Sentinel-2 MSI) produced much lower accuracy results, 0.642 in the best case. This form of validation could only be applied to a single image taken 3 days before the S1 image. A large number of false negatives would then be expected. A procedure developed to correct for this error gave an accuracy of 0.886 for this single event where this type of spatial validation was possible.

Another form of indirect validation was carried out. This consisted in attempting to relate the area flooded in each event to the amount of rainfall recorded. An RF regression model using both rainfall metrics and season of the year offered a correlation coefficient of

0.451 and RMSE = 979 ha in LOO-CV. This result shows a clear relationship between flooded areas and rainfall metrics. This result should not be interpreted as a predictive model for estimating the area flooded from precipitation; flooding is a phenomenon that depends on several different, complex and multifaceted factors. The aim is to verify whether, despite the above, the relationship with precipitation is clear enough to support the proposed system for detecting flooded areas.. To the best of our knowledge, this is the first time that such a validation was carried out. Further efforts should be made to improve both classification and validation methods for this type of data and objective.

5. Conclusions

A supervised classification approach is more useful than thresholding methods when the objective is to find flooded areas after an event, as bimodality may be difficult to find. Random Forest and Random Forest increase in probability are good tools to obtain flooded areas. The accuracy values obtained with cross-validation show a high ability of such models to at least detect water bodies. In particular, Random Forest increase in probability, before and after the event, allows to reduce false positives due to very flat surfaces. In this particular study area, irrigation ponds provide a good opportunity to obtain water training polygons for SAR, as they are fixed objects on the land. It is even possible to check whether they were filled or not in MSI images taken on the same day. Either way, after a large rainfall event, they certainly contain enough water to provide a water response to SAR. However, it is difficult to calibrate and validate models of processes that appear and disappear in a matter of days, as happens with floods. Sentinel imagery has a temporal resolution of 5 days, MSI and SAR do not coincide in time, so it is not possible to be sure that the SAR image coincides with the moment of maximum flooding, and it is very difficult to assess evaporation and infiltration between a SAR and the nearest MSI images. These problems are likely to lead to an underestimation of accuracy when validating with S2 imagery, and it proves difficult to find S2 imagery close enough in time, cloud-free enough, and with a clear presence of flooded areas to use for validation. However, the results obtained are considered encouraging. Further work is needed to try to obtain better validation approaches to be sure of the results. In any case, temporal validation shows a correspondence between the flooded area and the rainfall data for the analyzed events.

Author Contributions: Conceptualization, F.A.-S.; methodology, F.A.-S.; software, F.A.-S. and G.M.-P.; validation, F.A.-S. and C.V.-R.; formal analysis, F.A.-S. and C.V.-R.; investigation, F.A.-S. and C.V.-R.; resources, F.A.-S. and C.V.-R.; data curation, C.V.-R. and G.M.-P.; writing—original draft preparation, F.A.-S.; writing—review and editing, F.A.-S. and C.V.-R.; visualization, F.A.-S. and G.M.-P.; supervision, F.A.-S.; project administration, F.A.-S.; funding acquisition, F.A.-S. All authors have read and agreed to the published version of the manuscript.

Funding: This research was funded the Grant TED2021-131131B-I00 funded by MICIU/AEI/10.13039/501100011033 and by the European Union NextGenerat onEU/PRTR.

Data Availability Statement: The data used in this study were downloaded from the ESA Sentinel programme website.

Conflicts of Interest: The authors declare no conflicts of interest.

Abbreviations

The following abbreviations are used in this manuscript:

RF	Random Forest
SAR	Synthetic Aperture Radar

References

1. Jongman, B.; Ward, P.; Aerts, J. Global exposure to river and coastal flooding: Long term trends and changes. *Global Environ. Chang.* **2012**, *22*, 823–835. [CrossRef]
2. Hallegatte, S.; Green, C.; Nicholls, R.; Corfee-Morlot, J. Future flood losses in major coastal cities. *Nat. Clim. Chang.* **2013**, *3*, 802–806. [CrossRef]
3. Muhadi, N.; Abdullah, A.; Bejo, S.; Mahadi, M.; Mijic, A. Image Segmentation Methods for Flood Monitoring System. *Water* **2020**, *12*, 1825. [CrossRef]
4. Roy, R.; Gain, A.; Hurlbert, M.; Samat, N.; Tan, M.; Chan, N. Designing adaptation pathways for flood-affected households in Bangladesh. *Environ. Dev. Sustain.* **2020**, *23* , 5386–5410. [CrossRef]
5. Pall, P.; Aina, T.; Stone, D.; Stott, P.; Nozawa, T.; Hilberts, A.; Lohmann, D.; Allen, M. Anthropogenic greenhouse gas contribution to flood risk in England and Wales in autumn 2000. *Nature* **2011**, *470*, 382–385. [CrossRef]
6. Simonovic, S.; Kundzewicz, Z.; Wright, N. Floods and the COVID-19 pandemic—A new double hazard problem. *WIREs Water* **2021**, *8*, e1509. [CrossRef]
7. Masson-Delmotte, V.; Zhai, P.; Pirani, A.; Connors, S.L.; Péan, C.; Berger, S.; Caud, N.; Chen, Y.; Goldfarb, L.; Gomis, M.I.; et al. *Climate Change 2021: The Physical Science Basis. Contribution of Working Group I to the Sixth Assessment Report of the Intergovernmental Panel on Climate Change; Technical Summary*; Cambridge University Press: Cambridge, UK, 2021. [CrossRef]
8. CRED. *A2023 Disasters in Numbers*; Technical Report; Centre for Research on the Epidemiology of Disasters (CRED): Brussels, Belgium, 2023.
9. Nabinejad, S.; Schüttrumpf, H. Flood risk management in arid and semi-arid areas: A comprehensive review of challenges, needs, and opportunities. *Water* **2023**, *15*, 3113. [CrossRef]
10. Dokić, D.; Gavran, M.; Gregić, M.; Gantner, V. The impact of trade balance of agri-food products on the state's ability to withstand the crisis. *HighTech Innov. J.* **2020**, *1*, 107–111. [CrossRef]
11. Zhang, X.; Chan, N.; Pan, B.; Ge, X.; Yang, H. Mapping Flood by the Object-Based Method Using Backscattering Coefficient and Interference Coherence of Sentinel-1 Time Series. *Sci. Total. Environ.* **2021**, *794*, 148388. [CrossRef]
12. Jongman, B.; Wagemaker, J.; Revilla-Romero, B.; De Perez, E. Early flood detection for rapid humanitarian response: Harnessing near real-time satellite and Twitter signals. *ISPRS Int. J. Geo Inf.* **2015**, *4*, 2246–2266. [CrossRef]
13. Shen, X.; Anagnostou, E.; Allen, G.; Brakenridge, G.; Kettner, A. Near-real-time non-obstructed flood inundation mapping using synthetic aperture radar. *Remote Sens. Environ.* **2019**, *221*, 302–315. [CrossRef]
14. McFeeters, S. The use of the Normalized Difference Water Index (NDWI) in the delineation of open water features. *Int. J. Remote Sens.* **1996**, *17*, 1425–1432. [CrossRef]
15. Xu, H. Modification of normalised difference water index (NDWI) to enhance open water features in remotely sensed imagery. *Int. J. Remote Sens.* **2006**, *27*, 3025–3033. [CrossRef]
16. Gu, Y.; Hunt, E.; Wardlow, B.; Basara, J.; Brown, J.; Verdin, J. Evaluation of MODIS NDVI and NDWI for vegetation drought monitoring using oklahoma mesonet soil moisture data. *Geophys. Res. Lett.* **2008**, *35*, 5. [CrossRef]
17. Qiao, C.; Luo, J.; Sheng, Y.; Shen, Z.; Zhu, Z.; Ming, D. An adaptive water extraction method from remote sensing image based on NDWI. *J. Indian Soc. Remote Sens.* **2012**, *40*, 421–433. [CrossRef]
18. Tao, S.; Fang, J.; Zhao, X.; Zhao, S.; Shen, H.; Hu, H.; Tang, Z.; Wang, Z.; Guo, Q. Rapid loss of lakes on the mongolian plateau. *Proc. Natl. Acad. Sci. USA* **2015**, *112*, 2281–2286. [CrossRef]
19. Yan, P.; Zhang, Y.; Zhang, Y. A Study on Information Extraction of Water System in Semi-arid Regions with the Enhanced Water Index (EWI) and GIS Based Noise Remove Techniques. *Remote Sens. Inf.* **2007**, *6*, 62–67.
20. Feyisa, G.; Meilby, H.; Fensholt, R.; Proud, S. Automated Water Extraction Index: A new technique for surface water mapping using Landsat imagery. *Remote Sens. Environ.* **2014**, *140*, 23–35. [CrossRef]
21. Gstaiger, V.; Huth, J.; Gebhardt, S.; Kuenzer, C.; Wehrmann, T. Multi-sensoral and automated derivation of inundated areas using TerraSAR-X and ENVISAT ASAR data. *Int. J. Remote Sens.* **2012**, *33*, 7291–7304. [CrossRef]
22. Lira, J. Segmentation and morphology of open water bodies from multispectral images. *Int. J. Remote Sens.* **2006**, *27*, 4015–4038. [CrossRef]
23. Ko, B.; Kim, H.; Nam, J. Classification of potential water bodies using Landsat 8 OLI and a combination of two boosted random forest classifiers. *Sensors* **2015**, *15*, 13763–13777. [CrossRef] [PubMed]
24. Sheng, Y.; Shah, C.; Smith, L. Automated image registration for hydrologic change detection in the lake-rich Arctic. *IEEE Geosci. Remote Sensing Lett.* **2008**, *5*, 414–418. [CrossRef]
25. Jiang, Z.; Qi, J.; Su, S.; Zhang, Z.; Wu, J. Water body delineation using index composition and HIS transformation. *Int. J. Remote Sens.* **2012**, *33*, 3402–3421. [CrossRef]
26. Sun, F.; Sun, W.; Chen, J.; Gong, P. Comparison and improvement of methods for identifying waterbodies in remotely sensed imagery. *Int. J. Remote Sens.* **2012**, *33*, 6854–6875. [CrossRef]

27. Verpoorter, C.; Kutser, T.; Tranvik, L. Automated mapping of water bodies using Landsat multispectral data. *Limnol. Oceanogr. Methods* **2012**, *10*, 1037–1050. [CrossRef]
28. Dong, Z.; Wang, G.; Amankwah, S.; Wei, X.; Hu, Y.; Feng, A. Monitoring the Summer Flooding in the Poyang Lake Area of China in 2020 Based on Sentinel-1 Data and Multiple Convolutional Neural Networks. *Int. J. Appl. Earth Obs. Geoinf.* **2021**, *102*, 102400. [CrossRef]
29. Long, S.; Fatoyinbo, T.; Policelli, F. Flood extent mapping for namibia using change detection and thresholding with SAR. *Environ. Res. Lett.* **2014**, *9*, 035002. [CrossRef]
30. Tian, H.; Wu, M.; Niu, Z.; Wang, C.; Zhao, X. Dryland crops recognition under complex planting structure based on radarsat-2 images. *Trans. Chin. Soc. Agric. Eng.* **2015**, *31*, 154–159.
31. Li, S.; Tan, H.; Liu, Z.; Zhou, Z.; Liu, Y.; Zhang, W.; Liu, K.; Qin, B. Mapping High Mountain Lakes Using Space-Borne Near-Nadir SAR Observations. *Remote Sens.* **2018**, *10*, 1418. [CrossRef]
32. Cui, J.; Zhang, X.; Wang, W.; Shen, Y. Integration of optical and SAR remote sensing images for crop-type mapping based on a novel object-oriented feature selection method. *Int. J. Agric. Biol. Eng.* **2020**, *13*, 178–190. [CrossRef]
33. Liang, D.; Guo, H.; Zhang, L.; Li, H.; Wang, X. Sentinel-1 EW Mode Dataset for Antarctica from 2014–2020 Produced by the CASEarth Cloud Service Platform. *Big Earth Data* **2022**, *6*, 385–400. [CrossRef]
34. Luo, X.; Hu, Z.; Liu, L. Investigating the seasonal dynamics of surface water over the Qinghai–Tibet Plateau using Sentinel-1 imagery and a novel gated multiscale ConvNet. *Int. J. Digit. Earth* **2023**, *16*, 1372–1394. [CrossRef]
35. Torres, R.; Snoeij, P.; Geudtner, D.; Bibby, D.; Davidson, M.; Attema, E.; Potin, P.; Rommen, B.; Floury, N.; Brown, M. Gmes Sentinel-1 mission. *Remote Sens. Environ.* **2012**, *120*, 9–24. [CrossRef]
36. Huth, J.; Gessner, U.; Klein, I.; Yesou, H.; Lai, X.; Oppelt, N.; Kuenzer, C. Analyzing water dynamics based on Sentinel-1 time series—a study at the Dongting Lake wetlands in China. *Remote Sens.* **2020**, *12*, 1761. [CrossRef]
37. Singha, M.; Dong, J.; Sarmah, S.; You, N.; Zhou, Y.; Zhang, G.; Xiao, X. Identifying floods and flood-affected paddy rice fields in Bangladesh based on Sentinel-1 imagery and Google Earth Engine. *ISPRS J. Photogramm. Remote Sens.* **2020**, *166*, 278–293. [CrossRef]
38. Gašparović, M.; Dobrinić, D. Comparative assessment of machine learning methods for urban vegetation mapping using multitemporal sentinel-1 imagery. *Remote Sens.* **2020**, *12*, 1952. [CrossRef]
39. Li, Y.; Martinis, S.; Wieland, M. Urban Flood Mapping with an Active Self-Learning Convolutional Neural Network Based on TerraSAR-X Intensity and Interferometric Coherence. *ISPRS J. Photogramm. Remote Sens.* **2019**, *152*, 178–191. [CrossRef]
40. Ordoyne, C.; Friedl, M. Using MODIS data to characterize seasonal inundation patterns in the Florida Everglades. *Remote Sens. Environ.* **2008**, *112*, 4107–4119. [CrossRef]
41. Mahdianpari, M.; Salehi, B.; F.Mohammadimanesh.; Motagh, M. Random forest wetland classification using ALOS-2 L-band, RADARSAT-2 C-band, and TerraSAR-X imagery. *ISPRS J. Photogramm. Remote Sens.* **2017**, *130*, 13–31. [CrossRef]
42. Mahdavi, S.; Salehi, B.; Granger, J.; Amani, M.; Brisco, B.; Huang, W. Remote sensing for wetland classification: A comprehensive review. *GISci. Remote Sens.* **2018**, *55*, 623–658. [CrossRef]
43. Bao, Y.; Lin, L.; Wu, S.; Deng, K.; Petropoulos, G. Surface soil moisture retrievals over partially vegetated areas from the synergy of Sentinel-1 and Landsat 8 data using a modified water-cloud model. *Int. J. Appl. Earth Obs. Geoinf.* **2018**, *72*, 76–85. [CrossRef]
44. Tian, H.; Li, W.; Wu, M.; Huang, N.; Li, G.; Li, X.; Niu, Z. Dynamic Monitoring of the Largest Freshwater Lake in China Using a New Water Index Derived from High Spatiotemporal Resolution Sentinel-1A Data. *Remote Sens.* **2017**, *9*, 521. [CrossRef]
45. Oberstadler, R.; Hönsch, H.; Huth, D. Assessment of the mapping capabilities of ERS-1 SAR data for flood mapping: A case study in Germany. *Hydrol. Process.* **1997**, *11*, 1415–1425. [CrossRef]
46. Bazi, Y.; Bruzzone, L.; Melgani, F. An unsupervised approach based on the generalized Gaussian model to automatic change detection in multitemporal SAR images. *IEEE Trans. Geosci. Remote Sens.* **2005**, *43*, 874–887. [CrossRef]
47. Hostache, R. Estimation de niveaux d'eau en plaine inondée à partir d'images satellites radar et de données topographiques fines. *Revue Télédétection (Remote Sens. J.)* **2006**, *6*, 325–343.
48. Pierdicca, N.; Chini, M.; Pulvirenti, L.; Macina, F. Integrating physical and topographic information into a fuzzy scheme to map flooded area by SAR. *Sensors* **2008**, *8*, 4151–4164. [CrossRef]
49. Chini, M.; Piscini, A.; Cinti, F.; Amici, S.; Nappi, R.; DeMartini, P. The 2011 Tohoku (Japan) tsunami inundation and liquefaction investigated through optical, thermal, and SAR data. *IEEE Geosci. Remote Sens. Lett.* **2013**, *10*, 347–351. [CrossRef]
50. Schumann, G.; Hostache, R.; Puech, C.; Hoffmann, L.; Matgen, P.; Pappenberger, F.; Pfister, L. High-resolution 3-D flood information from radar imagery for flood hazard management. *IEEE Trans. Geosci. Remote Sens.* **2007**, *45*, 1715–1725. [CrossRef]
51. Chini, M.; Pelich, R.; Pulvirenti.; Pierdicca, N.; Hostache, R.; Matgen, P. Sentinel-1 InSAR coherence to detect floodwater in urban areas: Houston and Hurricane Harvey as a test case. *Remote Sens.* **2019**, *11*, 107. [CrossRef]
52. Chini, M.; Hostache, R.; Giustarini, L.; Matgen, P. A hierarchical split-based approach for parametric thresholding of SAR images: Flood inundation as a test case. *IEEE Trans. Geosci. Remote Sens.* **2017**, *55*, 6975–6988. [CrossRef]

53. Twele, A.; Cao, W.; Plank, S.; Martinis, S. Sentinel-1-based flood mapping: A fully automated processing chain. *Int. J. Remote Sens.* **2016**, *37*, 2990–3004. [CrossRef]
54. De Roo, A.; Van Der Knijff, J.; Horritt, M.; Schmuck, G.; De Jong, S., Assessing flood damages of the 1997 Oder flood and the 1995 Meuse flood. In *Proceedings of the Second International ITC Symposium on Operationalization of Remote Sensing*; Enschede, The Netherlands, 1999; pp. 16–20.
55. Townsend, P. Relationships between forest structure and the detection of flood inundation in forested wetlands using C-band SAR. *Int. J. Remote Sens.* **2002**, *23*, 443–460. [CrossRef]
56. Pulvirenti, L.; Pierdicca, N.; Chini, M.; Guerriero, L. Monitoring flood evolution in vegetated areas using COSMO-SkyMed data: The Tuscany 2009 case study. *IEEE J. Sel. Topics Appl. Earth Observ. Remote Sens.* **2013**, *6*, 1807–1816. [CrossRef]
57. Liang, J.; Liu, D. A local thresholding approach to flood water delineation using Sentinel-1 SAR imagery. *ISPRS J. Photogramm. Remote Sens.* **2020**, *159*, 53–62. [CrossRef]
58. Otsu, N. A Threshold Selection Method from Gray-Level Histograms. *IEEE Trans. Syst. Cybern.* **1979**, *9*, 62–66. [CrossRef]
59. Han, B.; Wu, Y. A novel active contour model driven by J-divergence entropy for SAR river image segmentation. *Pattern Anal. Appl.* **2018**, *21*, 613–627. [CrossRef]
60. Huo, W.; Huang, Y.; Pei, J.; Zhang, Q.; Gu, Q.; Yang, J. Ship detection from ocean SAR image based on local contrast variance weighted information entropy. *Sensors* **2018**, *18*, 1196. [CrossRef]
61. Huang, W.; DeVries, B.; Huang, C.; Lang, M.; Jones, J.; Creed, I.; Carroll, M. Automated Extraction of Surface Water Extent from Sentinel-1 Data. *Remote Sens.* **2018**, *10*, 797. [CrossRef]
62. Insom, P.; Cao, C.; Boonsrimuang, P.; Liu, D.; Saokarn, A.; Yomwan, P.; Xu, Y. A Support Vector Mawchine-Based Particle Filter Method for Improved Flooding Classification. *IEEE Geosci. Remote. Sens. Lett.* **2015**, *12*, 1943–1947. [CrossRef]
63. Skakun, S. A Neural Network Approach to Flood Mapping Using Satellite Imagery. *Comput. Inform.* **2010**, *29*, 1013–1024.
64. Zeng, L.; Schmitt, M.; Li, L.; Zhu, X. Analysing Changes of the Poyang Lake Water Area Using Sentinel-1 Synthetic Aperture Radar Imagery. *Int. J. Remote. Sens.* **2017**, *38*, 7041–7069. [CrossRef]
65. Mason, D.; Speck, R.; Devereux, B.; Schumann, G.; Neal, J.; Bates, P. Flood detection in urban areas using TerraSAR-X. *IEEE Trans. Geosci. Remote Sens.* **2010**, *48*, 882–894. [CrossRef]
66. Mason, D.; Schumann, G.; Neal, J.; Garcia-Pintado, J.; Bates, P. Automatic near real-time selection of flood water levels from high resolution Synthetic Aperture Radar images for assimilation into hydraulic models: A case study. *Remote Sens. Environ.* **2012**, *124*, 705–716. [CrossRef]
67. O'Grady, D.; Leblanc, M.; Gillieson, D. Use of ENVISAT ASAR Global Monitoring Mode to complement optical data in the mapping of rapid broad-scale flooding in Pakistan. *Hydrol. Earth Syst.* **2011**, *15*, 3475–3494. [CrossRef]
68. Martinis, S.; Twele, A.; Voigt, S. Towards operational near real-time flood detection using a split-based automatic thresholding procedure on high resolution TerraSAR-X data. *Nat. Hazard. Earth Syst. Sci.* **2009**, *9*, 303–314. [CrossRef]
69. Giustarini, L.; Hostache, R.; Kavetski, D.; Chini, M.; Corato, G.; Schlaffer, S.; Matgen, P. Probabilistic flood mapping using synthetic aperture radar data. *IEEE Trans. Geosci. Remote Sens.* **2016**, *54*, 6958–6969. [CrossRef]
70. Pulvirenti, L.; Chini, M.; Pierdicca, N.; Guerriero, L.; Ferrazzoli, P. Flood monitoring using multi-temporal COSMO-SkyMed data: Image segmentation and signature interpretation. *Remote Sens. Environ.* **2011**, *115*, 990–1002. [CrossRef]
71. Matgen, P.; Hostache, R.; Schumann, G.; Pfister, L.; Hoffmann, L.; Savenije, H. Towards an automated SAR-based flood monitoring system: Lessons learned from two case studies. *Phys. Chem. Earth* **2011**, *36*, 241–252. [CrossRef]
72. Tong, X.; Luo, X.; Liu, S.; Xie, H.; Chao, W.; Liu, S.; Liu, S.; Makhinov, A.; Makhinova, A.; Jiang, Y. An Approach for Flood Monitoring by the Combined use of Landsat 8 Optical Imagery and COSMO-SkyMed Radar Imagery. *ISPRS J. Photogramm. Remote Sens.* **2018**, *136*, 144–153. [CrossRef]
73. Cazals, C.; Rapinel, S.; Frison, P.; Bonis, A.; Mercier, G.; Mallet, C.; Corgne, S.; Rudant, J. Mapping and characterization of hydrological dynamics in a Coastal Marsh Using High Temporal Resolution Sentinel-1A Images. *Remote Sens.* **2016**, *8*, 570. [CrossRef]
74. Bhardwaj, A.; Singh, M.; Joshi, P.; Snehmani.; Singh, S.; Sam, L.; Gupta, R.; Kumar, R. A lake detection algorithm (LDA) using Landsat 8 data: A comparative approach in glacial environment. *Int. J. Appl. Earth Obs. Geoinf.* **2015**, *38*, 150–163. [CrossRef]
75. Sheng, Y.; Song, C.; Wang, J.; Lyons, E.; Knox, B.; Cox, J.; Gao, F. Representative lake water extent mapping at continental scales using multi-temporal Landsat-8 imagery. *Remote Sens. Environ.* **2016**, *185*, 129–141. [CrossRef]
76. Jiang, H.; Feng, M.; Zhu, Y.; Lu, N.; Huang, J.; Xiao, T. An automated method for extracting rivers and lakes from Landsat imagery. *Remote Sens.* **2014**, *6*, 5067–5089. [CrossRef]
77. Yang, K.; Li, M.; Liu, Y.; Cheng, L.; Huang, Q.; Chen, Y. River detection in remotely sensed imagery using Gabor filtering and path opening. *Remote Sens.* **2015**, *7*, 8779–8802. [CrossRef]
78. Li, W.; Gong, P. Continuous monitoring of coastline dynamics in western Florida with a 30-year time series of Landsat imagery. *Remote Sens. Environ.* **2016**, *179*, 196–209. [CrossRef]

79. Wang, D.; Cui, X.; Xie, F.; Jiang, Z.; Shi, Z. Multi-feature sea–land segmentation based on pixel-wise learning for optical remote-sensing imagery. *Int. J. Remote Sens.* **2017**, *38*, 4327–4347. [CrossRef]
80. Yang, X.; Qin, Q.; Grussenmeyer, P.; Koehl, M. Urban surface water body detection with suppressed built-up noise based on water indices from Sentinel-2 MSI imagery. *Remote Sens. Environ.* **2018**, *219*, 259–270. [CrossRef]
81. Ngoc, D.; Loisel, H.; Jamet, C.; Vantrepotte, V.; Duforêt-Gaurier, L.; Minh, C.; Mangin, A. Coastal and inland water pixels extraction algorithm (WiPE) from spectral shape analysis and HSV transformation applied to Landsat 8 OLI and Sentinel-2 MSI. *Remote Sens. Environ.* **2019**, *223*, 208–228. [CrossRef]
82. Cai, Y.; Li, X.; Zhang, M.; Lin, H. Mapping wetland using the object-based stacked generalization method based on multi-temporal optical and SAR data. *Int. J. Appl. Earth Obs. Geoinf.* **2020**, *92*, 102164. [CrossRef]
83. Hossain, M.; Chen, D. Segmentation for Object-Based Image Analysis (OBIA): A review of algorithms and challenges from remote sensing perspective. *ISPRS J. Photogramm. Remote Sens.* **2019**, *150*, 115–134. [CrossRef]
84. Phiri, D.; Morgenroth, J.; Xu, C.; Hermosilla, T. Effects of pre-processing methods on Landsat OLI-8 land cover classification using OBIA and random forests classifier. *Int. J. Appl. Earth Obs. Geoinf.* **2018**, *73*, 170–178. [CrossRef]
85. Isikdogan, F.; Bovik, A.; Passalacqua, P. Surface Water Mapping by Deep Learning. *IEEE J. Sel. Top. Appl. Earth Obs. Remote Sens.* **2017**, *10*, 4909–4918. [CrossRef]
86. Isikdogan, L.; Bovik, A.; Passalacqua, P. Seeing through the clouds with deepwatermap. *IEEE Geosci. Remote Sens. Lett.* **2019**, *17*, 1662–1666. [CrossRef]
87. Fang, W.; Wang, C.; Chen, X.; Wan, W.; Li, H.; Zhu, S.; Fang, Y.; Liu, B.; Hong, Y. Recognizing global reservoirs from landsat 8 images: A deep learning approach. *RIEEE J. Sel. Top. Appl. Earth Obs. Remote Sens.* **2019**, *12*, 3168–3177. [CrossRef]
88. Luo, X.; Tong, X.; Hu, Z. An Applicable and Automatic Method for Earth Surface Water Mapping Based on Multispectral Images. *Int. J. Appl. Earth Obs. Geoinf.* **2021**, *103*, 102472. [CrossRef]
89. Jiang, W.; He, G.; Long, T.; Ni, Y.; Liu, H.; Peng, Y.; Lv, K.; Wang, G. Multilayer Perceptron Neural Network for Surface Water Extraction in Landsat 8 OLI Satellite Images. *Remote Sens.* **2018**, *10*, 755. [CrossRef]
90. Romero Díaz, A.; Belmonte Serrato, F.; Hernández Bastida, J. El Campo de Cartagena una visión global. *Recorridos por el Campo de Cartagena. Control de la Degradación y uso Sostenible del Suelo*; Instituto Mediterráneo del Agua: Murcia, Spain, 2011; pp. 17–48.
91. CARM. Estadística Agraria de Murcia. 2022–2023. Technical Report, Comunidad Autónoma de la Región de Murcia. 2023. Available online: https://esam.carm.es/wp-content/uploads/2024/10/ESTADISTICA-AGRARIA-DE-MURCIA2022-2023-rev1.pdf (accessed on 29 January 2024).
92. Martínez, J.; Esteve, M.; Martínez-Paz, J.; Carreño, F.; Robledano, F.; Ruiz, M.; Alonso, F. Simulating management options and scenarios to control nutrient load to Mar Menor, Southeast Spain. *Transitional Waters Monogr. TWM Transit. Waters Monogr* **2007**, *1*. [CrossRef]
93. Giménez-Casalduero, F.; Gomariz-Castillo, F.; Alonso-Sarría, F.; Cortés, E.; Izquierdo-Muñoz, A.; Ramos-Esplá, A. Pinna nobilis in the Mar Menor coastal lagoon: A story of colonization and uncertainty. *Mar. Ecol. Prog. Ser.* **2020**, *652*, 77–94. [CrossRef]
94. Pérez Morales, A.; Romero Díaz, A.; Caballero Pedraza, A. The Urbanisation Process and its Influence on the Increase in Flooding (Region of Murcia, Campo de Cartagena-Mar Menor, South-east Spain). In *Crisis, Globalizations and Social and Regional Imbalances in Spain*; Asociación de Geógrafos Españolas (AGE): Madrid, Spain, 2016; pp. 92–103.
95. Pérez-Morales, A.; Gil-Guirado, S.; Olcina-Cantos, J. Housing bubbles and the increase of flood exposure. Failures in flood risk management on the Spanish south-eastern coast (1975–2013). *J. Flood Risk Manag.* **2015**, *2015*, S302–S313. [CrossRef]
96. MITECO. *Informe de Seguimiento del Plan de Gestión del Riesto de Inundación de la Demarcación Hidrográfica del Segura*; Technical Report; Ministerio para la Transición Ecológica y el Reto Demográfico. Gobierno de España.: Madrid, Spain, 2019.
97. Cortés-Melendreras, E.; Gomariz-Castillo, F.; Alonso-Sarría, F.; Martín, F.J.G.; Murcia, J.; Canales-Cáceres, R.; Esplá, A.A.R.; Barberáe, C.; Giménez-Casalduero, F. The relict population of Pinna nobilis in the Mar Menor is facing an uncertain future. *Mar. Pollut. Bull.* **2022**, *185*, 114376. [CrossRef]
98. European Space Agency. *Sentinel-2 Data*; Technical Report, European Space Agency: Paris, France, 2023.
99. Lang, M.W.; Townsend, P.A.; Kasischke, E.S. Influence of incidence angle on detecting flooded forests using C-HH synthetic aperture radar data. *Remote Sens. Environ.* **2008**, *112*, 3898–3907. [CrossRef]
100. Filipponi, F. Sentinel-1 GRD preprocessing workflow. *Proceedings* **2019**, *18*, 11. [CrossRef]
101. Breiman, L. Random Forests. *Mach. Learn.* **2001**, *45*, 5–32. [CrossRef]
102. Masís, S. *Interpretable Machine Learning with Python*; Packt Publishing: Birmingham, UK, 2021; p. 715.
103. Chen, Y.; Qiao, S.; Zhang, G.; Xu, Y.; Chen, L. Wu, L. Investigating the potential use of Sentinel-1 data for monitoring wetland water level changes in China's Momoge National Nature Reserve. *PeerJ* **2020**, *8*, 20.